J. Fluid Mech. (2020), *vol.* 897, A9. © The Author(s), 2020.

Published by Cambridge University Press
doi:10.1017/jfm.2020.375

Dynamics and invariants of the perceived velocity gradient tensor in homogeneous and isotropic turbulence

Ping-Fan Yang[1], **Alain Pumir**[2,3] **and Haitao Xu**[4,†]

[1]Center for Combustion Energy and Department of Energy and Power Engineering, Tsinghua University, 100084 Beijing, PR China

[2]Laboratoire de Physique, Ecole Normale Supérieure de Lyon, CNRS, Université de Lyon, 69007 Lyon, France

[3]Max Planck Institute for Dynamics and Self-Organization, Am Fassberg 17, 37077 Göttingen, Germany

[4]Center for Combustion Energy and School of Aerospace Engineering, Tsinghua University, 100084 Beijing, PR China

(Received 22 December 2019; revised 30 April 2020; accepted 1 May 2020)

The perceived velocity gradient tensor (PVGT), constructed from four fluid tracers forming a tetrahedron, provides a natural way to study the structure of velocity fluctuations and its dependence on spatial scales. It generalizes and shares qualitatively many properties with the true velocity gradient tensor. Here, we establish the evolution equation for the PVGT, and, for homogeneous and isotropic incompressible turbulent flows, we analyse the dynamics of the PVGT in particular using its second- and third-order invariants. We show that, for PVGT based on regular tetrads with lateral size R_0, the second-order invariants can be expressed solely in terms of the usual second-order velocity structure functions, while the third-order invariants involve the usual third-order longitudinal velocity structure function and a less well known three-point velocity correlation function. For homogeneous and isotropic turbulence, exact relations between the second moments of strain and vorticity, as well as enstrophy production and the third moments of the strain, are derived. These generalized relations are valid for all ranges of R_0, and reduce to classical results for the velocity gradient tensor when R_0 is in the dissipative range. With the help of these relations, we quantify the importance of the various terms, such as vortex stretching, as a function of the scale R_0. Our analysis, which is supported by the results of direct numerical simulations of turbulent flows in the Reynolds-number range $100 \leqslant R_\lambda \leqslant 610$, allows us to demonstrate that strain prevails over vorticity when R_0 is in the inertial range.

Key words: isotropic turbulence, turbulence theory

1. Introduction

The challenge to describe the physics of turbulent flows comes not only from the wide range of scales involved, but also from the spatial organization of the flow, which

† Email address for correspondence: hxu@tsinghua.edu.cn

https://doi.org/10.1017/jfm.2020.375 Published online by Cambridge University Press

is responsible for the coupling between scales (Monin & Yaglom 1975; Frisch 1995; Pope 2000). One manifestation of this complex structure is the emergence of tubes, where the magnitude of the vorticity vector $\boldsymbol{\omega} = \nabla \times \boldsymbol{U}$ is very high (Siggia 1981; Douady, Couder & Brachet 1991; Jimenez *et al.* 1993; Ishihara *et al.* 2007; Buaria *et al.* 2019). The amplification of vorticity results from its nonlinear coupling with the rate-of-strain tensor, $\boldsymbol{s} = \frac{1}{2}(\boldsymbol{m} + \boldsymbol{m}^{\mathrm{T}})$, where $\boldsymbol{m} = \nabla \boldsymbol{U}$ is the velocity gradient tensor (Frisch 1995; Tsinober 2009).

Much of the experimental investigation of turbulent flows has relied on the investigation of the velocity structure functions, defined as the moments of the difference between the component of flow velocity, $\boldsymbol{U}$, at two spatial points separated by a distance $\boldsymbol{x}$ along a spatial direction (say x): $D_n(x) = \langle (U(x) - U(0))^n \rangle$. While this quantity, defined with the help of two spatial points, is accessible from wind tunnel experiments (Comte-Bellot & Corrsin 1966; Pope 2000; Bodenschatz *et al.* 2014) and provides a very useful characterization of the scaling properties of the flow, it does not provide much information on the structural aspects of the velocity field. This deficiency is particularly important in the context of modelling the energy flux acting at small scales below the filtering scale in a large-eddy simulation approach (Borue & Orszag 1998; Tao, Katz & Meneveau 2002; Van der Bos *et al.* 2002; Meneveau 2011; Johnson & Meneveau 2018). A possible approach to studying simultaneously the structural and the scaling aspects of turbulence consists in considering the velocity at four points separated by a distance R_0 forming a regular tetrad (Chertkov, Pumir & Shraiman 1999). How such a tetrad deforms as the fluid particles move with the flow reveals interesting properties of the flow (Pumir, Shraiman & Chertkov 2000; Biferale *et al.* 2005; Naso & Pumir 2005; Xu, Ouellette & Bodenschatz 2008; Hackl, Yeung & Sawford 2011; Meneveau 2011; Xu, Pumir & Bodenschatz 2011; Naso & Godeferd 2012; Devenish 2013; Devenish & Thomson 2013; Sawford, Pope & Yeung 2013; Naso 2019). Here, we focus on the perceived velocity gradient tensor (PVGT), $\boldsymbol{M}$, obtained from the velocity differences over the distance between the four points defining the tetrad. The PVGT can be viewed as an extension of the velocity gradient tensor to length scales beyond the dissipation range (Chevillard & Meneveau 2006; Meneveau 2011; Jucha *et al.* 2014; Johnson & Meneveau 2016; Xu, Pumir & Bodenschatz 2016). Other attempts to study the velocity gradient beyond the dissipative scale include the velocity gradient coarse-grained over a spherical volume following a fluid particle trajectory (Meneveau & Lund 1994), and the velocity gradient obtained from the velocities of fluid particles within a sphere centred at a target fluid particle (Lüthi *et al.* 2007). As we stress in this work, the study of the PVGT provides some information on the relative role of vorticity and strain as a function of scales, and also on their dynamics.

As shown, for example, by Pumir, Bodenschatz & Xu (2013), strong similarities exist between the properties of the PVGT and those of the true velocity gradient $\boldsymbol{m}$. Nonetheless, there are important differences between the two quantities. One of them comes from the incompressibility condition, which is not satisfied by $\boldsymbol{M}$: $\mathrm{tr}(\boldsymbol{M}) \neq 0$, except in the limit $R_0 \to 0$, where $\boldsymbol{M}$ reduces to $\boldsymbol{m}$. This leads to quantitative differences in the properties of $\boldsymbol{m}$ and $\boldsymbol{M}$, which we analyse in this work.

Specifically, we decompose the PVGT as $\boldsymbol{M} = \boldsymbol{S} + \boldsymbol{W} + \frac{1}{3}\mathrm{tr}(\boldsymbol{M})\,\boldsymbol{I}$, where $\boldsymbol{S}$ and $\boldsymbol{W}$ are the symmetric and antisymmetric parts of $\boldsymbol{M}$, respectively, and $\boldsymbol{I}$ is the identity tensor. We establish here the evolution equations for $\boldsymbol{M}$, $\boldsymbol{S}$ and $\boldsymbol{W}$. The equations for the quadratic invariants of $\boldsymbol{M}$, $\mathrm{tr}(\boldsymbol{S}^2)$ and $\mathrm{tr}(\boldsymbol{W}^2)$, differ from the corresponding invariants of $\boldsymbol{m}$ via terms involving the traces of powers of $\boldsymbol{M}$. In the case of homogeneous turbulence in incompressible flows, the averaged values of $\mathrm{tr}(\boldsymbol{m}^2)$ and $\mathrm{tr}(\boldsymbol{m}^3)$ are

https://doi.org/10.1017/jfm.2020.375 Published online by Cambridge University Press

exactly zero (Betchov 1956). In fact, these relations allow one to express the second and third invariants of $\boldsymbol{m}$ in terms of $\langle \mathrm{tr}(\boldsymbol{s}^2)\rangle$ and $\langle \mathrm{tr}(\boldsymbol{s}^3)\rangle$ only. The deviation from the incompressibility ($\mathrm{tr}(\boldsymbol{M}) \neq 0$) makes the situation more complicated for the PVGT. In this work, we generalize the exact relations obtained in Betchov (1956) to the PVGT when the flow is homogeneous and isotropic, and, together with the dynamic equations for $\boldsymbol{M}$, we discuss quantitatively the production of strain rate and vorticity. Overall, we find that strain rate prevails over vorticity in the inertial range.

In technical terms, we show how to express the second- and third-order moments of the tensor $\boldsymbol{M}$ in terms of the second- and third-order correlation functions of the fluctuating velocity. In the case of an isotropic flow, this leads in turn to explicit asymptotic forms for most of the second and third moments of $\boldsymbol{M}$ in terms of the velocity structure functions. We stress that, whereas the original work of Betchov (1956) relied only on the incompressibility and homogeneity of the flow, the generalized relations are derived in this work by assuming that the flow is homogeneous and isotropic.

This work is organized as follows. In § 2, we recall the definition of $\boldsymbol{M}$, which is based on a general tetrad with arbitrary shape, and derive its evolution equation from the Navier–Stokes equations. Then § 3 generalizes the properties of the second and third moments of the true velocity gradient, $\boldsymbol{m}$, to the PVGT, $\boldsymbol{M}$, constructed from regular tetrahedra, and provides exact expressions for all the quantities involved, in the spirit of Betchov (1956), valid only for homogeneous and isotropic flows. Whereas our analysis relates most of these moments to the well-documented two-point longitudinal structure functions of the second and third order (Frisch 1995), the vortex stretching term also involves the genuine three-point correlation function, with three points on an equilateral triangle. In § 4, we express the correlations involving the PVGT, $\boldsymbol{M}$, and the fluid acceleration, appearing in the dynamics of the second and third moments of $\boldsymbol{M}$, in terms of the two-point velocity structure functions $D_n(r)$. Last, with the help of direct numerical simulation (DNS) data at several Reynolds numbers, we analyse in § 5 the various terms in the equations for strain and vorticity production, and show the prevalence of strain over vorticity production in the inertial range. Finally, § 6 presents our concluding remarks.

2. The perceived velocity gradient tensor

In this section, we discuss the definition of the PVGT $\boldsymbol{M}$ based on four fluid points in the flow, and derive the equation of evolution for $\boldsymbol{M}$. Our approach is completely general, and can be applied to tetrahedra of any shape. We will restrict ourselves to regular tetrahedra, defined by a set of four points separated from each other by a size R_0 only in later sections.

2.1. *Elementary construction of the perceived velocity gradient tensor*

We first introduce the convention used in this work. The construction of the PVGT used here closely follows previous work (Xu *et al.* 2011; Pumir *et al.* 2013). Consider four fluid particles in a homogeneous turbulent flows. We compute the PVGT $\boldsymbol{M}$ as follows. Denoting the positions and velocities of the four points in the laboratory frame by $\boldsymbol{X}^\alpha$ and $\boldsymbol{U}^\alpha$ ($\alpha = 1, 2, 3, 4$), respectively, we introduce the coordinates $\boldsymbol{x}^\alpha$ with respect to the centre of mass, $\boldsymbol{x}^\alpha = \boldsymbol{X}^\alpha - \boldsymbol{X}^0$, where $\boldsymbol{X}^0 = \frac{1}{4}\sum_{\alpha=1}^4 \boldsymbol{X}^\alpha$, and the reduced velocity, $\boldsymbol{u}^\alpha = \boldsymbol{U}^\alpha - \boldsymbol{U}^0$, where $\boldsymbol{U}^0 = \frac{1}{4}\sum_{\alpha=1}^4 \boldsymbol{U}^\alpha$. The PVGT $\boldsymbol{M}$, based on the four points of the tetrahedron, is defined by

$$x_j^\alpha M_{ji} = u_i^\alpha \quad \text{for } \alpha = 1, 2, 3, 4, \tag{2.1}$$

https://doi.org/10.1017/jfm.2020.375 Published online by Cambridge University Press

or equivalently, after multiplying both terms of (2.1) by x_k^α, and summing over α,

$$M_{ij} = g_{ik}^{-1} \Xi_{kj}, \tag{2.2}$$

where the tensors $\boldsymbol{g}$ and $\boldsymbol{\Xi}$ are defined by

$$g_{ij} \equiv \sum_{\alpha=1}^{4} x_i^\alpha x_j^\alpha \quad \text{and} \quad \Xi_{ij} \equiv \sum_{\alpha=1}^{4} x_i^\alpha u_j^\alpha. \tag{2.3\textit{a,b}}$$

When the tetrahedron is regular, the tensor $\boldsymbol{g}$ is isotropic, $g_{ij} = \frac{1}{3}\,\mathrm{tr}(\boldsymbol{g})\delta_{ij}$, with trace $\mathrm{tr}(\boldsymbol{g}) = \frac{3}{2}R_0^2$, where R_0 is the distance between any two points forming the tetrahedron. For a tetrahedron with arbitrary shape, we extend the definition of the scale R_0 to it by using

$$R_0^2 \equiv \frac{2}{3}\,\mathrm{tr}(\boldsymbol{g}) = \frac{2}{3}\sum_{\alpha=1}^{4} x_i^\alpha x_i^\alpha. \tag{2.4}$$

It is important to note that, contrary to the velocity gradient tensor $\boldsymbol{m}$, which is always incompressible, $\mathrm{tr}(\boldsymbol{m}) = 0$, the PVGT is in general not incompressible, $\mathrm{tr}(\boldsymbol{M}) \neq 0$. This reflects the observation that, at the level of the tetrad, the flow can locally lead to compression or expansion. In the following, we consider the trace of the tensor separately. We also consider the classical decomposition of the PVGT as a sum of its symmetric and antisymmetric parts,

$$M_{ij} = S_{ij} + W_{ij} + \tfrac{1}{3}\,\mathrm{tr}(\boldsymbol{M})\delta_{ij}, \tag{2.5}$$

where $S_{ij} = \frac{1}{2}(M_{ij} + M_{ji}) - \frac{1}{3}\,\mathrm{tr}(\boldsymbol{M})\delta_{ij}$ and $W_{ij} = \frac{1}{2}(M_{ij} - M_{ji})$. The $\boldsymbol{S}$ and $\boldsymbol{W}$ terms in (2.5) describe the straining and rotational motions as perceived by the four points of the tetrad. The definition simplifies in the case of the true velocity gradient tensor to $\boldsymbol{m} = \boldsymbol{s} + \boldsymbol{w}$. Given the definitions used here, the PVGT $\boldsymbol{M}$ reduces to the velocity gradient tensor $\boldsymbol{m}$ when the size of the tetrahedron, R_0, is vanishingly small. In practice, this limit is reached when R_0 is smaller than the Kolmogorov length scale $\eta = (\nu^3/\varepsilon)^{1/4}$, where ε is the rate of kinetic energy dissipation per unit mass in the flow (Pumir *et al.* 2013).

2.2. *Evolution equation for the perceived velocity gradient tensor*

The equation of evolution for $\boldsymbol{M}$ can be derived from (2.1)–(2.3). Namely, taking the time derivatives of (2.2) and (2.3) in the frame attached to $\boldsymbol{X}_0$ and moving with the centre-of-mass velocity $\boldsymbol{U}_0$ yields

$$\frac{\mathrm{d}g_{ik}}{\mathrm{d}t}M_{kj} + g_{ik}\frac{\mathrm{d}M_{kj}}{\mathrm{d}t} = \frac{\mathrm{d}\Xi_{ij}}{\mathrm{d}t} = \sum_{\alpha=1}^{4} u_i^\alpha u_j^\alpha + \sum_{\alpha=1}^{4} x_i^\alpha a_j^\alpha, \tag{2.6}$$

where $\boldsymbol{a}^\alpha$ is the accelerations of fluid particles relative to the centre of mass, which is related to the acceleration in the laboratory frame $\boldsymbol{A}^\alpha$ by $\boldsymbol{a}^\alpha = \boldsymbol{A}^\alpha - \frac{1}{4}\sum_{\beta=1}^{4}\boldsymbol{A}^\beta$. The Navier–Stokes equation express that

$$\boldsymbol{A}^\alpha = \frac{\mathrm{d}\boldsymbol{U}^\alpha}{\mathrm{d}t} = -\nabla P^\alpha + \boldsymbol{F}^\alpha + \nu\nabla^2\boldsymbol{U}^\alpha, \tag{2.7}$$

where $\boldsymbol{F}$ is the external body force per unit mass.

https://doi.org/10.1017/jfm.2020.375 Published online by Cambridge University Press

In (2.6) we can rewrite the term $\sum_{\alpha=1}^{4} u_i^\alpha u_j^\alpha$ in terms of $\boldsymbol{M}$ and $\boldsymbol{g}$ as

$$\sum_{\alpha=1}^{4} u_i^\alpha u_j^\alpha = \sum_{\alpha=1}^{4} x_k^\alpha M_{ki} x_n^\alpha M_{nj} = M_{ki} g_{kn} M_{nj} = \boldsymbol{M}^{\mathrm{T}} \boldsymbol{g} \boldsymbol{M}. \tag{2.8}$$

Differentiating $\boldsymbol{g}$, as defined by (2.3), with respect to time, leads to

$$\frac{\mathrm{d}\boldsymbol{g}}{\mathrm{d}t} = \boldsymbol{g}\boldsymbol{M} + \boldsymbol{M}^{\mathrm{T}}\boldsymbol{g}. \tag{2.9}$$

Then substituting (2.8) and (2.9) into (2.6) leads to, after some elementary algebra,

$$\begin{aligned}\frac{\mathrm{d}\boldsymbol{M}}{\mathrm{d}t} &= \boldsymbol{g}^{-1}[-\boldsymbol{g}\boldsymbol{M}^2 - \boldsymbol{M}^{\mathrm{T}}\boldsymbol{g}\boldsymbol{M} + \boldsymbol{M}^{\mathrm{T}}\boldsymbol{g}\boldsymbol{M} + \boldsymbol{H}/\mathrm{tr}(\boldsymbol{g}^{-1})] = -\boldsymbol{M}^2 + \boldsymbol{\Pi}\boldsymbol{H} \\ &= -\boldsymbol{M}^2 + \boldsymbol{\Pi}\boldsymbol{H}^p + \boldsymbol{\Pi}\boldsymbol{H}^\nu + \boldsymbol{\Pi}\boldsymbol{H}^f.\end{aligned} \tag{2.10}$$

Here the tensor $\boldsymbol{\Pi} = \boldsymbol{g}^{-1}/\mathrm{tr}(\boldsymbol{g}^{-1})$ was introduced by Chertkov *et al.* (1999) and $\boldsymbol{H}$ is defined by

$$H_{ij} = \mathrm{tr}(\boldsymbol{g}^{-1}) \sum_{\alpha=1}^{4} x_i^\alpha a_j^\alpha = H_{ij}^p + H_{ij}^\nu + H_{ij}^f, \tag{2.11}$$

in which H_{ij}^p, H_{ij}^ν and H_{ij}^f are the contributions to H_{ij} from the components of $\boldsymbol{a}^\alpha$ corresponding to the pressure gradient, the viscous forces and the external forcing; see (2.7). Equation (2.10) is very reminiscent of the evolution equation of $\boldsymbol{m}$ (Meneveau 2011):

$$\frac{\mathrm{d}\boldsymbol{m}}{\mathrm{d}t} = -\boldsymbol{m}^2 - \boldsymbol{\mathcal{H}}^p + \nu\nabla^2\boldsymbol{m} + \nabla\boldsymbol{F}, \tag{2.12}$$

where $\boldsymbol{\mathcal{H}}^p$ is the pressure Hessian, $\mathcal{H}_{ij}^p = \partial_i\partial_j p$. The strong resemblance between equations (2.10) and (2.12) is a direct consequence of the Navier–Stokes equations themselves. Namely, the quadratic nonlinear terms in (2.10) and (2.12) are identical, and the terms $\boldsymbol{\Pi}\boldsymbol{H}^p$, $\boldsymbol{\Pi}\boldsymbol{H}^\nu$ and $\boldsymbol{\Pi}\boldsymbol{H}^f$ in (2.10) represent the pressure Hessian, the viscous diffusion and the gradient of the external forcing in (2.12), respectively.

To simplify the notation in the analysis, we denote throughout the rest of the text the trace of a tensor by a bar over the tensor:

$$\overline{\boldsymbol{Y}} \equiv \mathrm{tr}(\boldsymbol{Y}). \tag{2.13}$$

Decomposing $\boldsymbol{M}$ as in (2.5), we readily obtain the equations for $\overline{\boldsymbol{M}}$, $\boldsymbol{S}$ and $\boldsymbol{W}$:

$$\frac{\mathrm{d}\overline{\boldsymbol{M}}}{\mathrm{d}t} = -\left(\overline{\boldsymbol{S}^2} + \overline{\boldsymbol{W}^2} + \frac{1}{3}\overline{\boldsymbol{M}}^2\right) + \overline{\boldsymbol{\Pi}\boldsymbol{H}}, \tag{2.14}$$

$$\frac{\mathrm{d}\boldsymbol{S}}{\mathrm{d}t} = -\boldsymbol{S}^2 - \boldsymbol{W}^2 - \frac{2}{3}\overline{\boldsymbol{M}}\boldsymbol{S} + \frac{1}{3}(\overline{\boldsymbol{S}^2} + \overline{\boldsymbol{W}^2})\boldsymbol{I} + \frac{1}{2}[\boldsymbol{\Pi}\boldsymbol{H} + (\boldsymbol{\Pi}\boldsymbol{H})^{\mathrm{T}}] - \frac{1}{3}\overline{\boldsymbol{\Pi}\boldsymbol{H}}\boldsymbol{I}, \tag{2.15}$$

$$\frac{\mathrm{d}\boldsymbol{W}}{\mathrm{d}t} = -\boldsymbol{S}\boldsymbol{W} - \boldsymbol{W}\boldsymbol{S} - \frac{2}{3}\overline{\boldsymbol{M}}\boldsymbol{W} + \frac{1}{2}[\boldsymbol{\Pi}\boldsymbol{H} - (\boldsymbol{\Pi}\boldsymbol{H})^{\mathrm{T}}], \tag{2.16}$$

where we recall that $\boldsymbol{I}$ refers to the identity tensor. The evolution equations for $\boldsymbol{m}$ and $\boldsymbol{M}$ differ in several important ways. The first important difference is that $\overline{\boldsymbol{M}}$ is,

https://doi.org/10.1017/jfm.2020.375 Published online by Cambridge University Press

in general, non-zero. This is made explicit in the decomposition (2.5), and results in terms involving $\overline{\boldsymbol{M}}$ in (2.15) and (2.16). The second difference comes from the appearance of a pressure term $\overline{\boldsymbol{\Pi} \boldsymbol{H}^p - (\boldsymbol{\Pi} \boldsymbol{H}^p)^{\mathrm{T}}}$ in the equation for $\boldsymbol{W}$ through the term $\overline{\boldsymbol{\Pi} \boldsymbol{H} - (\boldsymbol{\Pi} \boldsymbol{H})^{\mathrm{T}}}$, while the pressure does not contribute to the equation for the antisymmetric part $\boldsymbol{w}$ of the velocity gradient tensor $\boldsymbol{m}$:

$$\frac{\mathrm{d}\boldsymbol{w}}{\mathrm{d}t} = -\boldsymbol{s}\boldsymbol{w} - \boldsymbol{w}\boldsymbol{s} + \nu \nabla^2 \boldsymbol{w} + \frac{1}{2}[\nabla \boldsymbol{F} - (\nabla \boldsymbol{F})^{\mathrm{T}}]. \tag{2.17}$$

This effect of pressure originates from the finite difference approximation, and the term $\overline{\boldsymbol{\Pi} \boldsymbol{H}^p - (\boldsymbol{\Pi} \boldsymbol{H}^p)^{\mathrm{T}}}$ reduces to zero only in the $R_0 \to 0$ limit. Last, the coupling between the evolution of $\boldsymbol{M}$ and the geometry, through the tensor $\boldsymbol{g}$, leads to the most significant difference. As a result of this coupling, the evolution of $\boldsymbol{M}$ is not determined by (2.10) alone, as the shape and size of the tetrads evolve along with $\boldsymbol{M}$.

Taking into account these deformations is essential in the understanding of the physics of the PVGT (Pumir *et al.* 2013). In particular, equations (2.15) and (2.16) provide a way to investigate the production of strain rate and vorticity, and their dependence on scale. To quantify the production of vorticity and strain, we will particularly focus on the equations for the invariants $\langle \overline{\boldsymbol{S}^2} \rangle$ and $\langle \overline{\boldsymbol{W}^2} \rangle$, where the brackets $\langle \cdot \rangle$ denote an ensemble average over many tetrads with the same geometry in the flow. Multiplying (2.15) by $\boldsymbol{S}$, taking the trace and using the relation $\overline{\boldsymbol{S}} = 0$, we obtain

$$\frac{1}{2}\frac{\mathrm{d}\langle \overline{\boldsymbol{S}^2} \rangle}{\mathrm{d}t} = -\langle \overline{\boldsymbol{S}^3} \rangle - \langle \overline{\boldsymbol{W}\boldsymbol{S}\boldsymbol{W}} \rangle - \frac{2}{3}\langle \overline{\boldsymbol{M}}\, \overline{\boldsymbol{S}^2} \rangle + \langle \overline{\boldsymbol{\Pi}\boldsymbol{H}\boldsymbol{S}} \rangle. \tag{2.18}$$

Similarly, multiplying (2.16) by $\boldsymbol{W}$ leads to

$$\frac{1}{2}\frac{\mathrm{d}\langle \overline{\boldsymbol{W}^2} \rangle}{\mathrm{d}t} = -2\langle \overline{\boldsymbol{W}\boldsymbol{S}\boldsymbol{W}} \rangle - \frac{2}{3}\langle \overline{\boldsymbol{M}}\, \overline{\boldsymbol{W}^2} \rangle + \langle \overline{\boldsymbol{\Pi}\boldsymbol{H}\boldsymbol{W}} \rangle. \tag{2.19}$$

For tetrads of size R_0 much smaller than the Kolmogorov scale η, equation (2.19) reduces to the well-known equation for the evolution of enstrophy:

$$\frac{\mathrm{d}\langle \frac{1}{2}\boldsymbol{\omega}^2 \rangle}{\mathrm{d}t} = -\frac{\mathrm{d}\langle \overline{\boldsymbol{w}^2} \rangle}{\mathrm{d}t} = 4\langle \overline{\boldsymbol{w}\boldsymbol{s}\boldsymbol{w}} \rangle + \nu \langle \boldsymbol{\omega} \boldsymbol{\cdot} \nabla^2 \boldsymbol{\omega} \rangle + \langle \boldsymbol{\omega} \boldsymbol{\cdot} \nabla \times \boldsymbol{F} \rangle, \tag{2.20}$$

where the vorticity $\boldsymbol{\omega}$ is related to the antisymmetric part of $\boldsymbol{m}$ by $w_{ij} = -\frac{1}{2}\epsilon_{ijk}\omega_k$, with ϵ_{ijk} being the permutation tensor. We have made explicit use in (2.20) of the relation $\boldsymbol{\omega}^2 = -2\overline{\boldsymbol{w}^2}$, and we further note that $\overline{\boldsymbol{w}\boldsymbol{s}\boldsymbol{w}} = \frac{1}{4}\boldsymbol{\omega} \boldsymbol{\cdot} \boldsymbol{s} \boldsymbol{\cdot} \boldsymbol{\omega}$.

The coupling between the PVGT and the geometry, i.e. terms $\langle \overline{\boldsymbol{\Pi}\boldsymbol{H}\boldsymbol{S}} \rangle$ and $\langle \overline{\boldsymbol{\Pi}\boldsymbol{H}\boldsymbol{W}} \rangle$, implies that the averages of the time derivatives of the quadratic invariants, $-\boldsymbol{W}^2$ and $\boldsymbol{S}^2$, over many identical tetrads in the flow, are not zero, even if the flow is statistically stationary: vorticity or strain can grow, as measured by following an initially regular Lagrangian tetrad of size R_0. This property is interesting in its own right, as it allows us to characterize enstrophy and strain production as a function of scale.

As was the case for the velocity gradient tensor (Betchov 1956), a systematic analysis of the invariants of the PVGT, $\boldsymbol{M}$, helps in the understanding of the dynamics of vorticity and strain rate, as we document in the following section when $\boldsymbol{M}$ is based on regular tetrahedra. We stress that the relations established below are derived under the assumption that the turbulent fluctuations are locally isotropic, whereas the original Betchov derivation was based only on incompressibility and homogeneity.

https://doi.org/10.1017/jfm.2020.375 Published online by Cambridge University Press

3. Betchov relations generalized to the PVGT based on regular tetrahedra

In addition to the identity $\overline{\boldsymbol{m}} \equiv \mathrm{tr}(\boldsymbol{m}) = 0$, which simply results from incompressibility, it was established (Townsend 1951; Betchov 1956) that, in homogeneous flows,

$$\langle \overline{\boldsymbol{m}^2} \rangle = \langle \overline{\boldsymbol{m}^3} \rangle = 0. \tag{3.1}$$

These equalities result from elementary algebraic manipulations, and lead to the following identities:

$$\langle \overline{\boldsymbol{s}^2} \rangle = -\langle \overline{\boldsymbol{w}^2} \rangle = \tfrac{1}{2}\langle \boldsymbol{\omega}^2 \rangle, \tag{3.2}$$

$$\langle \overline{\boldsymbol{s}^3} \rangle = -3\langle \overline{\boldsymbol{wsw}} \rangle = -\tfrac{3}{4}\langle \boldsymbol{\omega} \boldsymbol{\cdot} \boldsymbol{s} \boldsymbol{\cdot} \boldsymbol{\omega} \rangle. \tag{3.3}$$

Equation (3.2) connects the amplitudes of vorticity and the rate of strain, while (3.3), remarkably, relates the rate of generation of enstrophy, $\langle \boldsymbol{\omega} \boldsymbol{\cdot} \boldsymbol{s} \boldsymbol{\cdot} \boldsymbol{\omega} \rangle$, see (2.20), to the properties of the rate of strain. Namely, equation (3.3) expresses the mean rate of generation of enstrophy in terms of the eigenvalues of $\boldsymbol{s}$, i.e. λ_1, λ_2 and λ_3 (ordered such that $\lambda_1 \geqslant \lambda_2 \geqslant \lambda_3$): $\langle \boldsymbol{\omega} \boldsymbol{\cdot} \boldsymbol{s} \boldsymbol{\cdot} \boldsymbol{\omega} \rangle = -4\langle \lambda_1\lambda_2\lambda_3 \rangle$. Enstrophy production implies that $\langle \lambda_1\lambda_2\lambda_3 \rangle < 0$, so the intermediate eigenvalue λ_2 is preferentially positive (Betchov 1956; Tsinober 2009).

In the rest of this section, assuming the flow to be statistically homogeneous and isotropic, we will extend relations (3.2) and (3.3) to the PVGT $\boldsymbol{M}$ obtained from regular tetrahedra.

The first step will be to establish relations between quantities $\overline{\boldsymbol{M}^n}$ for $n = 2$ and 3, generalizing (3.1). Based on equations (2.2), (2.3) and (3.4), we systematically reduce the moments of $\boldsymbol{M}$ to elementary moments of the velocity fluctuations at two or three points. We note that, for regular tetrads, equation (2.2) reduces to the simple form $\boldsymbol{M} = (2/R_0^2)\boldsymbol{\varXi}$, where $\boldsymbol{\varXi}$ is defined by (2.3). We also note that, with our definitions, the averaged value of $\overline{\boldsymbol{M}}$ vanishes,

$$\langle \overline{\boldsymbol{M}} \rangle = \frac{2}{R_0^2}\sum_{\alpha=1}^{4} x_i^\alpha \langle u_i^\alpha \rangle = 0, \tag{3.4}$$

as a consequence of the homogeneous condition $\langle u_i^\alpha \rangle = 0$ for any particle α $(1 \leqslant \alpha \leqslant 4)$ and for any component i $(1 \leqslant i \leqslant 3)$. While the second- and third-order velocity correlation functions involving two points separated by a given distance have been extensively studied (Monin & Yaglom 1975), it is interesting to note that the third-order moment of $\boldsymbol{M}$ involves the undocumented third-order velocity correlation function involving velocities at three points forming an equilateral triangle, which we need to evaluate.

3.1. *Second-order moments of M*

3.1.1. *Generalized Betchov relations for the second moments*

To simplify the notation, we denote the various second moments of $\boldsymbol{M}$ by T_2^p $(1 \leqslant p \leqslant 3)$, defined as

$$T_2^1 = \langle \overline{\boldsymbol{M}^2} \rangle, \quad T_2^2 = \langle \overline{\boldsymbol{M}\boldsymbol{M}^{\mathrm{T}}} \rangle \quad \text{and} \quad T_2^3 = \langle \overline{\boldsymbol{M}}^2 \rangle. \tag{3.5a–c}$$

The invariants such as $\langle \overline{\boldsymbol{S}^2} \rangle$ and $\langle \overline{\boldsymbol{W}^2} \rangle$ can be simply deduced from the equalities:

$$T_2^1 = \langle \overline{\boldsymbol{S}^2} \rangle + \langle \overline{\boldsymbol{W}^2} \rangle + \tfrac{1}{3}T_2^3, \quad \text{and} \quad T_2^2 = \langle \overline{\boldsymbol{S}^2} \rangle - \langle \overline{\boldsymbol{W}^2} \rangle + \tfrac{1}{3}T_2^3. \tag{3.6a,b}$$

https://doi.org/10.1017/jfm.2020.375 Published online by Cambridge University Press

To evaluate T_2^p, we start with (2.3) and (3.4). An elementary calculation leads to

$$T_2^1 = \left\langle \frac{4}{R_0^4}\overline{\boldsymbol{\varXi}}^2 \right\rangle = \left\langle \frac{4}{R_0^4}\left(\sum_{\alpha=1}^{4} x_i^\alpha u_j^\alpha\right)\left(\sum_{\beta=1}^{4} x_j^\beta u_i^\beta\right)\right\rangle$$
$$= \frac{4}{R_0^4}(4x_i^1\langle u_i^1 u_j^1\rangle x_j^1 + 12x_i^1\langle u_i^2 u_j^1\rangle x_j^2), \tag{3.7}$$

$$T_2^2 = \langle \overline{\boldsymbol{M}\boldsymbol{M}^{\mathrm{T}}}\rangle = \frac{2}{R_0^2}\left\langle \overline{\boldsymbol{M}^{\mathrm{T}}\frac{R_0^2}{2}\boldsymbol{I}\boldsymbol{M}}\right\rangle = \frac{2}{R_0^2}\langle\overline{\boldsymbol{M}^{\mathrm{T}}\boldsymbol{g}\boldsymbol{M}}\rangle$$
$$= \frac{2}{R_0^2}\left\langle \sum_{\alpha=1}^{4} u_i^\alpha u_i^\alpha \right\rangle = \frac{8}{R_0^2}\langle u_i^1 u_i^1\rangle, \tag{3.8}$$

$$T_2^3 = \left\langle \frac{4}{R_0^4}\overline{\boldsymbol{\varXi}^2} \right\rangle = \left\langle \frac{4}{R_0^4}\left(\sum_{\alpha=1}^{4} x_i^\alpha u_i^\alpha\right)\left(\sum_{\beta=1}^{4} x_j^\beta u_j^\beta\right)\right\rangle$$
$$= \frac{4}{R_0^4}(4x_i^1\langle u_i^1 u_j^1\rangle x_j^1 + 12x_i^1\langle u_i^1 u_j^2\rangle x_j^2). \tag{3.9}$$

To obtain the expressions of T_2^p in terms of the velocity correlations in the equations above, we used the symmetry between the vertices of a regular tetrahedron and the isotropy of the flow field, which lead to, for example, $x_i^1\langle u_i^1 u_j^1\rangle x_j^1 = x_i^2\langle u_i^2 u_j^2\rangle x_j^2$ and $x_i^1\langle u_i^1 u_j^2\rangle x_j^2 = x_i^3\langle u_i^3 u_j^4\rangle x_j^4$, and similar expressions by permuting the indices of the velocity $\boldsymbol{u}^\alpha$ and position, $\boldsymbol{x}^\beta$. We also note that the fourth equality in (3.8) results from (2.8). The second moments T_2^p are therefore expressed in terms of the two-point velocity correlation functions $\langle u_i^1 u_j^1\rangle$ and $\langle u_i^1 u_j^2\rangle$. To proceed, we note that, for homogeneous and isotropic velocity fields, the correlation tensor $\langle u_i(\boldsymbol{0})u_j(\boldsymbol{r})\rangle$ can be expressed as (see equation (12.30) of Monin & Yaglom (1975))

$$\langle u_i(\boldsymbol{0})u_j(\boldsymbol{r})\rangle = \mathscr{F}_1\hat{r}_i\hat{r}_j + \mathscr{F}_2\delta_{ij}, \tag{3.10}$$

where $\mathscr{F}_1$ and $\mathscr{F}_2$ are scalar functions of r ($r=|\boldsymbol{r}|$) and $\hat{\boldsymbol{r}}$ is the unit vector in the $\boldsymbol{r}$ direction. This implies, in particular, that $\langle u_i(\boldsymbol{0})u_j(\boldsymbol{r})\rangle$ is symmetric in its indices i and j, and therefore that $x_i^1\langle u_i^1 u_j^2\rangle x_j^2 = x_i^1\langle u_i^2 u_j^1\rangle x_j^2$. Then from (3.7) and (3.9), we conclude that $T_2^1 = T_2^3$, or in other words

$$\langle\overline{\boldsymbol{M}^2}\rangle = \langle\overline{\boldsymbol{M}}^2\rangle. \tag{3.11}$$

Substituting in (3.6) leads to

$$\langle\overline{\boldsymbol{S}^2}\rangle = -\langle\overline{\boldsymbol{W}^2}\rangle + \tfrac{2}{3}\langle\overline{\boldsymbol{M}}^2\rangle. \tag{3.12}$$

Equations (3.11) and (3.12) can be viewed as generalizations of (3.1) and (3.2) to the PVGT, for which $\overline{\boldsymbol{M}} \neq 0$. Obviously, equations (3.11) and (3.12) reduce to the classical expressions when R_0 is in the dissipative range, where $\overline{\boldsymbol{M}} = 0$.

https://doi.org/10.1017/jfm.2020.375 Published online by Cambridge University Press

3.1.2. *Expression of the second moments in terms of two-point structure functions*

For isotropic turbulent flows, the correlation functions $\langle u_i^\alpha u_j^\beta \rangle$ that appear in (3.7)–(3.9) can in fact be systematically expressed in terms of the second-order longitudinal velocity structure function

$$D_2(r) = \langle [(\boldsymbol{U}(\boldsymbol{r}) - \boldsymbol{U}(\boldsymbol{0})) \cdot \hat{\boldsymbol{r}}]^2 \rangle, \tag{3.13}$$

where $\boldsymbol{U}$ is the fluctuating turbulent velocity as defined in § 2.1. The velocity correlation tensor $\mathscr{R}_{ij}(\boldsymbol{r}) = \langle U_i(\boldsymbol{x}) U_j(\boldsymbol{x}+\boldsymbol{r}) \rangle$ can be written as (cf. § 6.2.1 of Davidson (2015) and equations (12.29) and (13.69) of Monin & Yaglom (1975))

$$\begin{aligned} \mathscr{R}_{ij}(\boldsymbol{r}) &= \mathscr{R}_1 \hat{r}_i \hat{r}_j + \mathscr{R}_2 \delta_{ij} & (3.14)\\ &= \frac{\hat{r}_i \hat{r}_j}{4} r D_2'(r) + \left[\frac{1}{3} \langle U^2 \rangle - \frac{D_2(r)}{2} - \frac{r}{4} D_2'(r) \right] \delta_{ij}, & (3.15) \end{aligned}$$

where the prime denotes the derivative with respect to r. Recall the relation between $\boldsymbol{u}$ and $\boldsymbol{U}$, $\boldsymbol{u}^\alpha = \boldsymbol{U}^\alpha - \frac{1}{4}(\sum_{\beta=1}^4 \boldsymbol{U}^\beta)$, and also that $\langle U_i^1 U_j^1 \rangle = \frac{1}{3} \langle U^2 \rangle \delta_{ij}$ and $\langle U_i^1 U_j^2 \rangle = \mathscr{R}_{ij}(\boldsymbol{r}^{12}) = \mathscr{R}_{ij}(\boldsymbol{x}^2 - \boldsymbol{x}^1)$, with $\boldsymbol{r}^{\alpha\beta} \equiv \boldsymbol{x}^\beta - \boldsymbol{x}^\alpha$. The correlations appearing in equations (3.7)–(3.9) can thus be expressed as

$$\begin{aligned} \langle u_i^1 u_i^1 \rangle &= \left\langle \left(U_i^1 - \frac{1}{4} \sum_{\beta=1}^4 U_i^\beta \right) \left(U_i^1 - \frac{1}{4} \sum_{\beta=1}^4 U_i^\beta \right) \right\rangle \\ &= \langle U_i^1 U_i^1 \rangle - \frac{2}{4} (\langle U_i^1 U_i^1 \rangle + 3 \langle U_i^1 U_i^2 \rangle) + \frac{1}{16} (4 \langle U_i^1 U_i^1 \rangle + 12 \langle U_i^1 U_i^2 \rangle) \\ &= \frac{3}{4} \langle U^2 \rangle - \frac{3}{4} \langle U_i^1 U_i^2 \rangle = \frac{3}{4} \langle U^2 \rangle - \frac{3}{4} (\mathscr{R}_1 + 3 \mathscr{R}_2) \\ &= \frac{9}{8} D_2(R_0) + \frac{3}{8} R_0 D_2'(R_0), & (3.16) \\ x_i^1 \langle u_i^1 u_j^1 \rangle x_j^1 &= x_i^1 \left\langle \left(U_i^1 - \frac{1}{4} \sum_{\beta=1}^4 U_i^\beta \right) \left(U_j^1 - \frac{1}{4} \sum_{\beta=1}^4 U_j^\beta \right) \right\rangle x_j^1 \\ &= \frac{3}{4} x_i^1 \langle U_i^1 U_j^1 \rangle x_j^1 - \frac{6}{4} x_i^1 \langle U_i^1 U_j^2 \rangle x_j^1 + \frac{6}{16} x_i^1 \langle U_i^1 U_j^2 \rangle x_j^1 + \frac{6}{16} x_i^1 \langle U_i^2 U_j^3 \rangle x_j^1 \\ &= \frac{1}{4} \langle U^2 \rangle x_i^1 x_i^1 - \frac{9}{8} x_i^1 x_j^1 \mathscr{R}_{ij}(\boldsymbol{x}^2 - \boldsymbol{x}^1) + \frac{3}{8} x_i^1 x_j^1 \mathscr{R}_{ij}(\boldsymbol{x}^3 - \boldsymbol{x}^2) \\ &= \frac{3}{32} \langle U^2 \rangle R_0^2 - \frac{9}{8} (x_i^1 x_j^1 \hat{r}_i^{12} \hat{r}_j^{12} \mathscr{R}_1 + x_i^1 x_i^1 \mathscr{R}_2) + \frac{3}{8} (x_i^1 x_j^1 \hat{r}_i^{23} \hat{r}_j^{23} \mathscr{R}_1 + x_i^1 x_i^1 \mathscr{R}_2) \\ &= \left(\frac{3}{32} \langle U^2 \rangle - \frac{9}{32} \mathscr{R}_1 - \frac{9}{32} \mathscr{R}_2 \right) R_0^2 = \frac{9}{64} D_2(R_0) R_0^2 & (3.17) \end{aligned}$$

and

$$\begin{aligned} x_i^1 \langle u_i^1 u_j^2 \rangle x_j^2 &= x_i^1 \left\langle \left(U_i^1 - \frac{1}{4} \sum_{\beta=1}^4 U_i^\beta \right) \left(U_j^2 - \frac{1}{4} \sum_{\beta=1}^4 U_j^\beta \right) \right\rangle x_j^2 \\ &= -\frac{1}{4} x_i^1 \langle U_i^1 U_j^1 \rangle x_j^2 + \frac{5}{8} x_i^1 \langle U_i^1 U_j^2 \rangle x_j^2 - \frac{8}{16} x_i^1 \langle U_i^1 U_j^3 \rangle x_j^2 + \frac{1}{8} x_i^1 \langle U_i^3 U_j^4 \rangle x_j^2 \end{aligned}$$

https://doi.org/10.1017/jfm.2020.375 Published online by Cambridge University Press

$$
\begin{aligned}
&= -\frac{1}{12}\langle U^2\rangle x_i^1 x_i^2 + \frac{5}{8}x_i^1 x_j^2 \mathscr{R}_{ij}(\boldsymbol{r}^{12}) - \frac{1}{2}x_i^1 x_j^2 \mathscr{R}_{ij}(\boldsymbol{r}^{13}) + \frac{1}{8}x_i^1 x_j^2 \mathscr{R}_{ij}(\boldsymbol{r}^{34}) \\
&= \frac{1}{96}\langle U^2\rangle R_0^2 + \frac{5}{8}x_i^1 x_j^2 \hat{r}_i^{12}\hat{r}_j^{12}\mathscr{R}_1 - \frac{1}{2}x_i^1 x_j^2 \hat{r}_i^{13}\hat{r}_j^{13}\mathscr{R}_1 + \frac{1}{8}x_i^1 x_j^2 \hat{r}_i^{34}\hat{r}_j^{34}\mathscr{R}_1 + \frac{1}{4}x_i^1 x_i^2 \mathscr{R}_2 \\
&= \left(\frac{1}{96}\langle U^2\rangle - \frac{5}{32}\mathscr{R}_1 - \frac{1}{32}\mathscr{R}_2\right) R_0^2 \\
&= \left[\frac{1}{64}D_2(R_0) - \frac{1}{32}R_0 D_2'(R_0)\right] R_0^2.
\end{aligned}
\tag{3.18}
$$

In the derivation of the results above, we made explicit use of the symmetry of the regular tetrahedron, and of the flow isotropy, as done in equations (3.7)–(3.9). A crucial element in our derivation is the geometric factors such as $x_i^\alpha x_j^\beta \hat{r}_i^{\gamma\delta}\hat{r}_j^{\gamma\delta}$, which can be expanded to multiplications of $x_i^\alpha x_i^\beta$, or the inner product between $\boldsymbol{x}^\alpha$ and $\boldsymbol{x}^\beta$. These quantities can be evaluated by taking into account that the tetrad under consideration is regular and that the coordinates of the vertices $\boldsymbol{x}^\alpha$ can be expressed, up to a rotation, as $(\pm 1/2, 0, -1/(2\sqrt{2}))R_0$ and $(0, \pm 1/2, 1/(2\sqrt{2}))R_0$, which leads to

$$
\boldsymbol{x}^\alpha \cdot \boldsymbol{x}^\beta = \begin{cases} \frac{3}{8}R_0^2, & \text{when } \alpha = \beta, \\ -\frac{1}{8}R_0^2, & \text{when } \alpha \neq \beta. \end{cases}
\tag{3.19}
$$

Expanding $x_i^\alpha x_j^\beta \hat{r}_i^{\gamma\delta}\hat{r}_j^{\gamma\delta}$ in terms of $x_i^\alpha x_i^\beta$, one obtains the following identities:

$$
x_i^\alpha x_j^\beta \hat{r}_i^{\gamma\delta}\hat{r}_j^{\gamma\delta} = \begin{cases} \frac{1}{4}R_0^2, & \text{if } \gamma \neq \delta \text{ and } (\alpha,\beta) = (\gamma,\gamma) \text{ or } (\alpha,\beta) = (\delta,\delta), \\ -\frac{1}{4}R_0^2, & \text{if } \gamma \neq \delta \text{ and } (\alpha,\beta) = (\gamma,\delta) \text{ or } (\alpha,\beta) = (\delta,\gamma), \\ 0, & \text{otherwise.} \end{cases}
\tag{3.20}
$$

With the help of these expressions, equations (3.7)–(3.9) reduce to

$$
\langle \overline{\boldsymbol{M}}^2 \rangle = \langle \overline{\boldsymbol{M}^2} \rangle = \frac{1}{R_0^2}\left(3D_2(R_0) - \frac{3}{2}R_0 D_2'(R_0)\right)
\tag{3.21}
$$

and

$$
\langle \overline{\boldsymbol{M}\boldsymbol{M}^{\mathrm{T}}} \rangle = \frac{1}{R_0^2}(9D_2(R_0) + 3R_0 D_2'(R_0)).
\tag{3.22}
$$

The expressions above can be further simplified by using the scaling properties of $D_2(r)$. In the inertial range of scales, $D_2(r) = C_2(\varepsilon r)^{2/3}$, so (3.22) and (3.21) together with (3.6) lead to

$$
\left.
\begin{aligned}
\langle \overline{\boldsymbol{M}}^2 \rangle = \langle \overline{\boldsymbol{M}^2} \rangle &= 2\frac{D_2(R_0)}{R_0^2}, \\
\langle \overline{\boldsymbol{M}\boldsymbol{M}^{\mathrm{T}}} \rangle &= 11\frac{D_2(R_0)}{R_0^2}, \\
\langle \overline{\boldsymbol{S}^2} \rangle &= \frac{35}{6}\frac{D_2(R_0)}{R_0^2}, \\
\langle \overline{\boldsymbol{W}^2} \rangle &= -\frac{9}{2}\frac{D_2(R_0)}{R_0^2},
\end{aligned}
\right\}
\tag{3.23}
$$

https://doi.org/10.1017/jfm.2020.375 Published online by Cambridge University Press

all for $\eta \ll R_0 \ll L$. In the dissipative range of scales, $D_2(r)$ reduces to $D_2(r) = \langle (m_{11})^2 \rangle r^2$, which yields

$$\left.\begin{aligned} \langle \overline{\boldsymbol{M}}^2 \rangle = \langle \overline{\boldsymbol{M}^2} \rangle = 0, \\ \langle \overline{\boldsymbol{M}\boldsymbol{M}^{\mathrm{T}}} \rangle = 15 \frac{D_2(R_0)}{R_0^2} = 15 \langle (m_{11})^2 \rangle, \\ \langle \overline{\boldsymbol{S}^2} \rangle = -\langle \overline{\boldsymbol{W}^2} \rangle = \frac{15}{2} \frac{D_2(R_0)}{R_0^2} = \frac{15}{2} \langle (m_{11})^2 \rangle, \end{aligned}\right\} \tag{3.24}$$

for $R_0 \ll \eta$. As anticipated, one recovers in this limit the classical Betchov relations, equations (3.1) and (3.2).

3.2. *Third-order moments of* $\boldsymbol{M}$

We now turn to the third-order moments of $\boldsymbol{M}$. As was the case for the second-order moments, we introduce the notation T_3^p as

$$T_3^1 = \langle \overline{\boldsymbol{M}}^3 \rangle, \quad T_3^2 = \langle \overline{\boldsymbol{M}^2 \boldsymbol{M}^{\mathrm{T}}} \rangle, \quad T_3^3 = \langle \overline{\boldsymbol{M}^2}\, \overline{\boldsymbol{M}} \rangle, \quad T_3^4 = \langle \overline{\boldsymbol{M}\boldsymbol{M}^{\mathrm{T}}}\, \overline{\boldsymbol{M}} \rangle, \quad \text{and} \quad T_3^5 = \langle \overline{\boldsymbol{M}^3} \rangle. \tag{3.25a–e}$$

We note that, using the decomposition of $\boldsymbol{M}$, the quantities T_3^p are related to moments of $\boldsymbol{S}$, $\boldsymbol{W}$ and $\overline{\boldsymbol{M}}$ as

$$T_3^1 = \langle \overline{\boldsymbol{M}}^3 \rangle = \langle \overline{\boldsymbol{M}}^3 \rangle, \tag{3.26}$$

$$T_3^2 = \langle \overline{\boldsymbol{M}^2 \boldsymbol{M}^{\mathrm{T}}} \rangle = \langle \overline{\boldsymbol{S}^3} \rangle - \langle \overline{\boldsymbol{W}\boldsymbol{S}\boldsymbol{W}} \rangle + \langle \overline{\boldsymbol{S}^2}\, \overline{\boldsymbol{M}} \rangle - \tfrac{1}{3} \langle \overline{\boldsymbol{W}^2}\, \overline{\boldsymbol{M}} \rangle + \tfrac{1}{9} \langle \overline{\boldsymbol{M}}^3 \rangle, \tag{3.27}$$

$$T_3^3 = \langle \overline{\boldsymbol{M}^2}\, \overline{\boldsymbol{M}} \rangle = \langle \overline{\boldsymbol{S}^2}\, \overline{\boldsymbol{M}} \rangle + \langle \overline{\boldsymbol{W}^2}\, \overline{\boldsymbol{M}} \rangle + \tfrac{1}{3} \langle \overline{\boldsymbol{M}}^3 \rangle, \tag{3.28}$$

$$T_3^4 = \langle \overline{\boldsymbol{M}\boldsymbol{M}^{\mathrm{T}}}\, \overline{\boldsymbol{M}} \rangle = \langle \overline{\boldsymbol{S}^2}\, \overline{\boldsymbol{M}} \rangle - \langle \overline{\boldsymbol{W}^2}\, \overline{\boldsymbol{M}} \rangle + \tfrac{1}{3} \langle \overline{\boldsymbol{M}}^3 \rangle, \tag{3.29}$$

$$T_3^5 = \langle \overline{\boldsymbol{M}^3} \rangle = \langle \overline{\boldsymbol{S}^3} \rangle + 3 \langle \overline{\boldsymbol{W}\boldsymbol{S}\boldsymbol{W}} \rangle + \langle \overline{\boldsymbol{S}^2}\, \overline{\boldsymbol{M}} \rangle + \langle \overline{\boldsymbol{W}^2}\, \overline{\boldsymbol{M}} \rangle + \tfrac{1}{9} \langle \overline{\boldsymbol{M}}^3 \rangle. \tag{3.30}$$

In homogeneous and isotropic turbulent flows, the corresponding quantities for R_0 in the dissipation range ($R_0 \lesssim \eta$), obtained by substituting $\boldsymbol{M}$ by $\boldsymbol{m}$ in the above definitions, all reduce to zero, except for T_3^2.

We now show that the quantities T_3^1, T_3^3 and T_3^5 are in fact related through a simple relation, which is a property of $\boldsymbol{M}$ for homogeneous and isotropic turbulence. This relation provides us with a generalization of the Betchov relation, equation (3.3), for $\boldsymbol{m}$ in homogeneous flows.

To proceed, we express, as done in § 3.1, the moments of the quantities T_3^p in terms of geometric factors such as $x_i^\alpha x_j^\beta x_k^\gamma$, multiplied by the third-order velocity correlation function, taken at two spatial points, $\mathscr{S}_{ijk}(\boldsymbol{r}) = \langle U_i(\boldsymbol{x}) U_j(\boldsymbol{x}) U_k(\boldsymbol{x}+\boldsymbol{r}) \rangle$, and the third-order velocity correlation function evaluated at three different spatial points forming an equilateral triangle, $\mathscr{Q}_{ijk}(\boldsymbol{\eta}, \boldsymbol{\xi}) = \langle U_i(\boldsymbol{x}) U_j(\boldsymbol{x}+\boldsymbol{\eta}) U_k(\boldsymbol{x}+\boldsymbol{\xi}) \rangle$. For incompressible isotropic fields, the third-order correlation at two spatial points, $\mathscr{S}_{ijk}$, can be expressed as (cf. § 6.2.1 of Davidson (2015) and equations (12.120) and (13.80) of Monin & Yaglom (1975))

$$\mathscr{S}_{ijk}(\boldsymbol{r}) = \mathscr{S}_1 \hat{r}_i \hat{r}_j \hat{r}_k + \mathscr{S}_2 (\hat{r}_i \delta_{jk} + \hat{r}_j \delta_{ik}) + \mathscr{S}_3 \hat{r}_k \delta_{ij} \tag{3.31}$$

$$= \frac{1}{6} \left[\frac{D_3(r) - r D_3'(r)}{2} \hat{r}_i \hat{r}_j \hat{r}_k + \frac{2 D_3(r) + r D_3'(r)}{4} (\hat{r}_i \delta_{jk} + \hat{r}_j \delta_{ik}) - \frac{D_3(r)}{2} \hat{r}_k \delta_{ij} \right], \tag{3.32}$$

https://doi.org/10.1017/jfm.2020.375 Published online by Cambridge University Press

where $D_3(r) = \langle [(\boldsymbol{U}(\boldsymbol{r}) - \boldsymbol{U}(\boldsymbol{0})) \boldsymbol{\cdot} \hat{\boldsymbol{r}}]^3 \rangle$ is the third-order longitudinal velocity structure function. On the other hand, the three-point correlation function $\mathcal{Q}_{ijk}$ is not so well known. Its general expression (see § 12.5 of Monin & Yaglom (1975)) is given by

$$\begin{aligned}\mathcal{Q}_{ijk}(\boldsymbol{\eta}, \boldsymbol{\xi}) = {} & \mathcal{Q}_1 \hat{\eta}_i \hat{\eta}_j \hat{\eta}_k + \mathcal{Q}_2 \hat{\eta}_i \delta_{jk} + \mathcal{Q}_3 \hat{\eta}_j \delta_{ik} \\ & + \mathcal{Q}_4 \hat{\eta}_k \delta_{ij} + \mathcal{Q}_5 \hat{\eta}_i \hat{\eta}_j \hat{\xi}_k + \mathcal{Q}_6 \hat{\eta}_i \hat{\xi}_j \hat{\eta}_k + \mathcal{Q}_7 \hat{\xi}_i \hat{\eta}_j \hat{\eta}_k \\ & + \mathcal{Q}_8 \hat{\xi}_i \hat{\xi}_j \hat{\eta}_k + \mathcal{Q}_9 \hat{\xi}_i \hat{\eta}_j \hat{\xi}_k + \mathcal{Q}_{10} \hat{\eta}_i \hat{\xi}_j \hat{\xi}_k + \mathcal{Q}_{11} \hat{\xi}_i \hat{\xi}_j \hat{\xi}_k \\ & + \mathcal{Q}_{12} \hat{\xi}_i \delta_{jk} + \mathcal{Q}_{13} \hat{\xi}_j \delta_{ik} + \mathcal{Q}_{14} \hat{\xi}_k \delta_{ij},\end{aligned} \tag{3.33}$$

where the $\mathcal{Q}_n$ are scalar functions of $|\boldsymbol{\xi}|$, $|\boldsymbol{\eta}|$ and $\boldsymbol{\xi} \boldsymbol{\cdot} \boldsymbol{\eta}$. Using the symmetric conditions $\mathcal{Q}_{ijk}(\boldsymbol{\eta}, \boldsymbol{\xi}) = \mathcal{Q}_{ikj}(\boldsymbol{\xi}, \boldsymbol{\eta}) = \mathcal{Q}_{jik}(-\boldsymbol{\eta}, \boldsymbol{\xi} - \boldsymbol{\eta})$, and noting that, for a regular tetrahedron, $|\boldsymbol{\xi}| = |\boldsymbol{\eta}| = |\boldsymbol{\xi} - \boldsymbol{\eta}| = R_0$ and $\boldsymbol{\xi} \boldsymbol{\cdot} \boldsymbol{\eta} = \boldsymbol{\xi} \boldsymbol{\cdot} (\boldsymbol{\xi} - \boldsymbol{\eta}) = \frac{1}{2} R_0^2$ (the three points involved in the definition of $\mathcal{Q}_{ijk}$ form an equilateral triangle), we can reduce the $\mathcal{Q}_n$ appearing in (3.33) to only three independent scalar functions:

$$\begin{aligned}\mathcal{Q}_{ijk}(\boldsymbol{\eta}, \boldsymbol{\xi}) = {} & \mathcal{Q}_1 \hat{\eta}_i \hat{\eta}_j \hat{\eta}_k + \mathcal{Q}_2 \hat{\eta}_i \delta_{jk} - 2\mathcal{Q}_2 \hat{\eta}_j \delta_{ik} \\ & + \mathcal{Q}_2 \hat{\eta}_k \delta_{ij} + \mathcal{Q}_5 \hat{\eta}_i \hat{\eta}_j \hat{\xi}_k - \tfrac{1}{2} \mathcal{Q}_1 \hat{\eta}_i \hat{\xi}_j \hat{\eta}_k - (\mathcal{Q}_1 + \mathcal{Q}_5) \hat{\xi}_i \hat{\eta}_j \hat{\eta}_k \\ & - \tfrac{1}{2} \mathcal{Q}_1 \hat{\xi}_i \hat{\xi}_j \hat{\eta}_k + \mathcal{Q}_5 \hat{\xi}_i \hat{\eta}_j \hat{\xi}_k - (\mathcal{Q}_1 + \mathcal{Q}_5) \hat{\eta}_i \hat{\xi}_j \hat{\xi}_k \\ & + \mathcal{Q}_1 \hat{\xi}_i \hat{\xi}_j \hat{\xi}_k + \mathcal{Q}_2 \hat{\xi}_i \delta_{jk} + \mathcal{Q}_2 \hat{\xi}_j \delta_{ik} - 2\mathcal{Q}_2 \hat{\xi}_k \delta_{ij}.\end{aligned} \tag{3.34}$$

Substituting equations (3.31) and (3.34) into (3.25) allows us to express T_3^p in terms of scalar functions $\mathcal{S}_n$ and $\mathcal{Q}_n$. Here we show briefly the derivation of T_3^5 as an example:

$$\begin{aligned} T_3^5 &= \left\langle \frac{8}{R_0^6} \overline{\boldsymbol{\varXi}^3} \right\rangle = \left\langle \frac{8}{R_0^6} \left(\sum_{\alpha=1}^{4} x_i^\alpha u_j^\alpha \right) \left(\sum_{\beta=1}^{4} x_j^\beta u_k^\beta \right) \left(\sum_{\gamma=1}^{4} x_k^\gamma u_i^\gamma \right) \right\rangle \\ &= \left\langle \frac{8}{R_0^6} \left(\sum_{\alpha=1}^{4} x_i^\alpha (U_j^\alpha - U_j^0) \right) \left(\sum_{\beta=1}^{4} x_j^\beta (U_k^\beta - U_k^0) \right) \left(\sum_{\gamma=1}^{4} x_k^\gamma (U_i^\gamma - U_i^0) \right) \right\rangle \\ &= \left\langle \frac{8}{R_0^6} \left(\sum_{\alpha=1}^{4} x_i^\alpha U_j^\alpha \right) \left(\sum_{\beta=1}^{4} x_j^\beta U_k^\beta \right) \left(\sum_{\gamma=1}^{4} x_k^\gamma U_i^\gamma \right) \right\rangle \\ &= \frac{8}{R_0^6} (4 x_i^1 x_j^1 x_k^1 \langle U_i^1 U_j^1 U_k^1 \rangle + 36 x_i^1 x_j^1 x_k^2 \langle U_j^1 U_k^1 U_i^2 \rangle + 24 x_i^1 x_j^2 x_k^3 \langle U_j^1 U_k^2 U_i^3 \rangle) \\ &= \frac{8}{R_0^6} [36 \mathcal{S}_{jki}(\boldsymbol{x}^2 - \boldsymbol{x}^1) x_i^1 x_j^1 x_k^2 + 24 \mathcal{Q}_{jki}(\boldsymbol{x}^2 - \boldsymbol{x}^1, \boldsymbol{x}^3 - \boldsymbol{x}^1)] x_i^1 x_j^2 x_k^3 \\ &= \frac{8}{R_0^6} \left[36 \times \left(\frac{1}{8} \mathcal{S}_1 + \frac{1}{4} \mathcal{S}_2 + \frac{1}{16} \mathcal{S}_3 \right) + 24 \times \left(\frac{3}{16} \mathcal{Q}_1 - \frac{3}{16} \mathcal{Q}_2 - \frac{1}{8} \mathcal{Q}_5 \right) \right] \times R_0^3 \\ &= (36 \mathcal{S}_1 + 72 \mathcal{S}_2 + 18 \mathcal{S}_3 + 36 \mathcal{Q}_1 - 36 \mathcal{Q}_2 + 24 \mathcal{Q}_5)/R_0^3. \end{aligned} \tag{3.35}$$

When obtaining the result above, for the first three equalities, we simply substituted in the definition of T_3^5 and expanded the expression. The fourth equality relies on the identity $\sum_{\alpha=1}^{4} x_i^\alpha = 0$ for any single tetrad. For the fifth equality, we used the isotropy of the velocity field and the symmetry between the vertices of the tetrahedra. The sixth equality comes from the definitions of $\mathcal{S}_{ijk}$ and $\mathcal{Q}_{ijk}$ and the isotropy of the flow

https://doi.org/10.1017/jfm.2020.375 Published online by Cambridge University Press

field so that the third-order moment of the single-point velocity fluctuation $\langle U_i^1 U_j^1 U_k^1\rangle$ vanishes. The seventh equality is obtained by substituting in equations (3.31) and (3.34) the expressions for $\mathscr{S}_{ijk}$ and $\mathscr{Q}_{ijk}$, and evaluating the geometric factors such as $\hat{r}_i\hat{r}_j\hat{r}_k x_i^1 x_j^1 x_k^1$, $\hat{r}_i\delta_{jk}x_i^1 x_j^1 x_k^1$, $\hat{\xi}_i\hat{\xi}_j\hat{\xi}_k x_i^1 x_j^1 x_k^1$, etc., which are all proportional to R_0^3. The last equality is obtained by rearranging the terms.

Other T_3^p are obtained in a similar way. Among all the steps involved, the evaluation of the geometric factors like $\hat{r}_i\hat{r}_j\hat{r}_k x_i^1 x_j^1 x_k^1$ involve some cumbersome algebra. We determined those expressions using formal calculation with MATLAB. The script is available upon request. In summary, the results are

$$\left.\begin{aligned} T_3^1 &= (36\mathscr{S}_1 + 36\mathscr{S}_2 + 54\mathscr{S}_3 + 72\mathscr{Q}_2 - 48\mathscr{Q}_5)/R_0^3,\\ T_3^2 &= (30\mathscr{S}_1 + 108\mathscr{S}_2 + 42\mathscr{S}_3 + 3\mathscr{Q}_1 - 24\mathscr{Q}_2 + 6\mathscr{Q}_5)/R_0^3,\\ T_3^3 &= (36\mathscr{S}_1 + 60\mathscr{S}_2 + 30\mathscr{S}_3 + 24\mathscr{Q}_1)/R_0^3,\\ T_3^4 &= (30\mathscr{S}_1 + 84\mathscr{S}_2 + 66\mathscr{S}_3 - 6\mathscr{Q}_1 + 48\mathscr{Q}_2 - 12\mathscr{Q}_5)/R_0^3,\\ T_3^5 &= (36\mathscr{S}_1 + 72\mathscr{S}_2 + 18\mathscr{S}_3 + 36\mathscr{Q}_1 - 36\mathscr{Q}_2 + 24\mathscr{Q}_5)/R_0^3. \end{aligned}\right\} \tag{3.36}$$

With these expressions, we note that the quantities T_3^1, T_3^3 and T_3^5 are related by $\frac{1}{2}T_3^1 - \frac{3}{2}T_3^3 + T_3^5 = 0$, i.e.

$$\langle\overline{\boldsymbol{M}^3}\rangle = \tfrac{3}{2}\langle\overline{\boldsymbol{M}^2}\,\overline{\boldsymbol{M}}\rangle - \tfrac{1}{2}\langle\overline{\boldsymbol{M}}^3\rangle. \tag{3.37}$$

Substitution of equations (3.26), (3.28) and (3.30) into (3.37) yields

$$\langle\overline{\boldsymbol{S}^3}\rangle = -3\langle\overline{\boldsymbol{WSW}}\rangle + \tfrac{1}{2}\langle\overline{\boldsymbol{M}}\,\overline{\boldsymbol{M}^2}\rangle - \tfrac{5}{18}\langle\overline{\boldsymbol{M}}^3\rangle. \tag{3.38}$$

Equations (3.37) and (3.38) generalize the Betchov relations to the PVGT. They reduce to the classical expressions (3.1) and (3.3) when R_0 is in the dissipative range of scales ($R_0 \lesssim \eta$).

We note that, contrary to the second-order moments T_2^p, defined by (3.5), which could be explicitly expressed in terms of the well-studied second-order velocity structure function, the invariants T_3^p cannot be reduced to the corresponding third-order structure function of the velocity difference between two points. Instead, they involve the three-point correlation functions based on three points forming an equilateral triangle, as shown by (3.36).

4. Mixed second-order invariants of $\boldsymbol{M}$ and $\boldsymbol{\Pi H}$

The evolution equations of the strain and enstrophy based on the PVGT, namely, equations (2.18) and (2.19), involve not only the third-order invariants of $\boldsymbol{M}$ due to nonlinearity, but also the mixed invariants of $\boldsymbol{M}$ and $\boldsymbol{\Pi H}$, which can be expressed in terms of $\langle\overline{\boldsymbol{M\Pi H}}\rangle$, $\langle\overline{\boldsymbol{M}(\boldsymbol{\Pi H})^{\mathrm{T}}}\rangle$ and $\langle\overline{\boldsymbol{M}}\,\overline{\boldsymbol{\Pi H}}\rangle$. The terms involved in (2.18) and (2.19) for the evolution of the strain and enstrophy, respectively $\langle\overline{\boldsymbol{\Pi HS}}\rangle$ and $\langle\overline{\boldsymbol{\Pi HW}}\rangle$, can be readily deduced from these terms, via the relations

$$\langle\overline{\boldsymbol{\Pi HS}}\rangle = \tfrac{1}{2}\langle\overline{\boldsymbol{M\Pi H}}\rangle + \tfrac{1}{2}\langle\overline{\boldsymbol{M}(\boldsymbol{\Pi H})^{\mathrm{T}}}\rangle - \tfrac{1}{3}\langle\overline{\boldsymbol{M}}\,\overline{\boldsymbol{\Pi H}}\rangle \tag{4.1}$$

and

$$\langle\overline{\boldsymbol{\Pi HW}}\rangle = \tfrac{1}{2}\langle\overline{\boldsymbol{M\Pi H}}\rangle - \tfrac{1}{2}\langle\overline{\boldsymbol{M}(\boldsymbol{\Pi H})^{\mathrm{T}}}\rangle. \tag{4.2}$$

https://doi.org/10.1017/jfm.2020.375 Published online by Cambridge University Press

As we now demonstrate, these terms can also be represented by the third-order longitudinal structure function $D_3(r)$. Expanding these terms by their definitions leads to

$$\langle \overline{\boldsymbol{M}(\boldsymbol{\Pi H})^{\mathrm{T}}} \rangle = \frac{8}{R_0^2} \langle u_i^1 a_i^1 \rangle, \tag{4.3}$$

$$\langle \overline{\boldsymbol{M}}\,\overline{\boldsymbol{\Pi H}} \rangle = \frac{4}{R_0^4} (4x_i^1 \langle u_i^1 a_j^1 \rangle x_j^1 + 12 x_i^1 \langle u_i^1 a_j^2 \rangle x_j^2), \tag{4.4}$$

$$\langle \overline{\boldsymbol{M \Pi H}} \rangle = \frac{4}{R_0^4} (4x_i^1 \langle u_i^1 a_j^1 \rangle x_j^1 + 12 x_i^1 \langle a_i^2 u_j^1 \rangle x_j^2), \tag{4.5}$$

in which the correlation between the reduced velocity $\boldsymbol{u}^\alpha$ and the reduced acceleration $\boldsymbol{a}^\beta$ can be related to the velocity–acceleration correlation function $\mathscr{L}_{ij}(\boldsymbol{r}) = \langle U_i(\boldsymbol{x}) A_j(\boldsymbol{x}+\boldsymbol{r}) \rangle$ through definitions $\boldsymbol{u}^\alpha = \boldsymbol{U}^\alpha - \frac{1}{4}\sum_{\beta=1}^4 \boldsymbol{U}^\beta$ and $\boldsymbol{a}^\alpha = \boldsymbol{A}^\alpha - \frac{1}{4}\sum_{\beta=1}^4 \boldsymbol{A}^\beta$. We also note that, for isotropic flows, $\mathscr{L}_{ij}$ can be written as

$$\mathscr{L}_{ij}(\boldsymbol{r}) = \mathscr{L}_1 \hat{r}_i \hat{r}_j + \mathscr{L}_2 \delta_{ij}, \tag{4.6}$$

in which $\mathscr{L}_1$ and $\mathscr{L}_2$ are scalar functions of r. With the help of (4.6), and using the symmetry of the vertices of the regular tetrads, we can evaluate the correlations involving $\langle u_i^\alpha a_j^\beta \rangle$ in terms of the velocity–acceleration correlation function as

$$\langle u_i^1 a_i^1 \rangle = \tfrac{3}{4} \langle U_i A_i \rangle - \tfrac{3}{4} (\mathscr{L}_1 + 3\mathscr{L}_2), \tag{4.7}$$

$$x_i^1 \langle u_i^1 a_j^1 \rangle x_j^1 = (\tfrac{3}{32} \langle U_i A_i \rangle - \tfrac{9}{32} \mathscr{L}_1 - \tfrac{9}{32} \mathscr{L}_2) R_0^2, \tag{4.8}$$

$$x_i^1 \langle u_j^1 a_i^2 \rangle x_j^2 = (\tfrac{1}{96} \langle U_i A_i \rangle - \tfrac{5}{32} \mathscr{L}_1 - \tfrac{1}{32} \mathscr{L}_2) R_0^2. \tag{4.9}$$

The stationarity of the flow implies that $\langle U_i A_i \rangle = \mathrm{d}\langle U^2 \rangle / \mathrm{d}t = 0$. We also note that the symmetry between the indices i and j leads to $\langle u_i^1 a_j^2 \rangle = \langle a_i^2 u_j^1 \rangle$.

To proceed, we need to derive tractable expressions for $\mathscr{L}_1$ and $\mathscr{L}_2$. To that end, we decompose the acceleration $\boldsymbol{A}$ as a sum of a local part $\partial \boldsymbol{U}/\partial t$, plus a convective part $\boldsymbol{U} \boldsymbol{\cdot} \boldsymbol{\nabla} \boldsymbol{U}$. This leads to

$$\begin{aligned} \mathscr{L}_{ij}(\boldsymbol{r}) &= \langle U_i(\boldsymbol{x}) A_j(\boldsymbol{x}+\boldsymbol{r}) \rangle \\ &= \left\langle U_i(\boldsymbol{x}) \frac{\partial U_j(\boldsymbol{x}+\boldsymbol{r})}{\partial t} \right\rangle + \left\langle U_i(\boldsymbol{x}) U_k(\boldsymbol{x}+\boldsymbol{r}) \frac{\partial U_j(\boldsymbol{x}+\boldsymbol{r})}{\partial (\boldsymbol{x}+\boldsymbol{r})_k} \right\rangle \\ &= \left\langle U_i(\boldsymbol{x}) \frac{\partial U_j(\boldsymbol{x}+\boldsymbol{r})}{\partial t} \right\rangle + \frac{\partial}{\partial r_k} \langle U_i(\boldsymbol{x}) U_k(\boldsymbol{x}+\boldsymbol{r}) U_j(\boldsymbol{x}+\boldsymbol{r}) \rangle. \end{aligned} \tag{4.10}$$

The first term on the right-hand side vanishes, since

$$\begin{aligned} 0 &= \frac{\partial}{\partial t} \langle U_i(\boldsymbol{x}) U_j(\boldsymbol{x}+\boldsymbol{r}) \rangle = \left\langle U_i(\boldsymbol{x}) \frac{\partial U_j(\boldsymbol{x}+\boldsymbol{r})}{\partial t} \right\rangle + \left\langle \frac{\partial U_i(\boldsymbol{x})}{\partial t} U_j(\boldsymbol{x}+\boldsymbol{r}) \right\rangle \\ &= 2 \left\langle U_i(\boldsymbol{x}) \frac{\partial U_j(\boldsymbol{x}+\boldsymbol{r})}{\partial t} \right\rangle, \end{aligned} \tag{4.11}$$

where the last equality comes from isotropy. Finally, since $\langle U_i(\boldsymbol{x}) U_k(\boldsymbol{x}+\boldsymbol{r}) U_j(\boldsymbol{x}+\boldsymbol{r}) \rangle = \mathscr{S}_{jki}(-\boldsymbol{r})$, we obtain from (4.10),

$$\mathscr{L}_{ij}(\boldsymbol{r}) = \frac{\partial}{\partial r_k} \mathscr{S}_{jki}(-\boldsymbol{r}). \tag{4.12}$$

https://doi.org/10.1017/jfm.2020.375 Published online by Cambridge University Press

Substituting equations (3.31) and (3.32) into the expression above, elementary manipulations lead to

$$\begin{aligned}\mathscr{L}_{ij}(\boldsymbol{r}) &= \mathscr{L}_1\hat{r}_i\hat{r}_j + \mathscr{L}_2\delta_{ij} \\ &= \left(\frac{-2\mathscr{S}_1}{r} - \mathscr{S}_1' + \frac{\mathscr{S}_2}{r} - \mathscr{S}_2' + \frac{\mathscr{S}_3}{r} - \mathscr{S}_3'\right)\hat{r}_i\hat{r}_j + \left(\frac{-3\mathscr{S}_2}{r} - \mathscr{S}_2' - \frac{\mathscr{S}_3}{r}\right)\delta_{ij} \\ &= \left(\frac{-D_3(r)}{6r} + \frac{D_3'(r)}{6} + \frac{D_3''(r)r}{24}\right)\hat{r}_i\hat{r}_j + \left(\frac{-D_3(r)}{6r} - \frac{D_3'(r)}{4} - \frac{D_3''(r)r}{24}\right)\delta_{ij}.\end{aligned} \tag{4.13}$$

Therefore, substituting equations (4.7)–(4.9) and (4.13) into equations (4.3)–(4.5), we obtain

$$\langle\overline{\boldsymbol{M}(\boldsymbol{\varPi}\boldsymbol{H})^{\mathrm{T}}}\rangle = \frac{4D_3(R_0)}{R_0} + \frac{7D_3'(R_0)}{2} + \frac{D_3''(R_0)R_0}{2}, \tag{4.14}$$

$$\langle\overline{\boldsymbol{M}\boldsymbol{\varPi}\boldsymbol{H}}\rangle = \langle\overline{\boldsymbol{M}}\,\overline{\boldsymbol{\varPi}\boldsymbol{H}}\rangle = \frac{3D_3(R_0)}{R_0} - \frac{D_3'(R_0)}{2} - \frac{D_3''(R_0)R_0}{4}. \tag{4.15}$$

Equations (4.14) and (4.15) can be further simplified by using the scaling properties of the structure function $D_3(r)$. For R_0 in the inertial range of scales, the celebrated four-fifths law, $D_3(R_0) = -\frac{4}{5}\varepsilon R_0$, implies that

$$\langle\overline{\boldsymbol{M}(\boldsymbol{\varPi}\boldsymbol{H})^{\mathrm{T}}}\rangle = \frac{15D_3(R_0)}{2R_0^3} = \frac{-6\varepsilon}{R_0^2} \tag{4.16}$$

and

$$\langle\overline{\boldsymbol{M}\boldsymbol{\varPi}\boldsymbol{H}}\rangle = \langle\overline{\boldsymbol{M}}\,\overline{\boldsymbol{\varPi}\boldsymbol{H}}\rangle = \frac{5D_3(R_0)}{2R_0^3} = \frac{-2\varepsilon}{R_0^2}. \tag{4.17}$$

When R_0 is in the dissipative range, $D_3(R_0) = \langle(m_{11})^3\rangle R_0^3$, which leads to

$$\langle\overline{\boldsymbol{M}(\boldsymbol{\varPi}\boldsymbol{H})^{\mathrm{T}}}\rangle = \frac{35D_3(R_0)}{2R_0^3} = \frac{35}{2}\langle(m_{11})^3\rangle \tag{4.18}$$

and

$$\langle\overline{\boldsymbol{M}\boldsymbol{\varPi}\boldsymbol{H}}\rangle = \langle\overline{\boldsymbol{M}}\,\overline{\boldsymbol{\varPi}\boldsymbol{H}}\rangle = 0. \tag{4.19}$$

It is interesting to recall that the acceleration $\boldsymbol{A}^\alpha$ can be decomposed as a sum of the pressure gradient, viscous dissipation and external forcing, see (2.7). The mixed second-order invariants of $\boldsymbol{M}$ and $\boldsymbol{\varPi}\boldsymbol{H}$ considered in this section can be divided into three parts, corresponding to the contribution from the external forcing term, the pressure gradient term and the viscous term. We expect the viscous term to dominate the other two, especially when the length scale is much smaller than the integral scale L. The arguments are that, first, $\langle U_i(\boldsymbol{x})\nabla_j P(\boldsymbol{x}+\boldsymbol{r})\rangle = 0$ due to isotropy and incompressibility (von Kármán & Howarth 1938) and, second, the external force $\boldsymbol{F}^\alpha$ is imposed on the large scale and varies moderately in the region we consider; thus $\boldsymbol{f}^\alpha = \boldsymbol{F}^\alpha - \frac{1}{4}\sum_{\beta=1}^{4}\boldsymbol{F}^\beta \approx 0$, which leads to $\langle u_i^\alpha f_j^\beta\rangle \approx 0$.

https://doi.org/10.1017/jfm.2020.375 Published online by Cambridge University Press

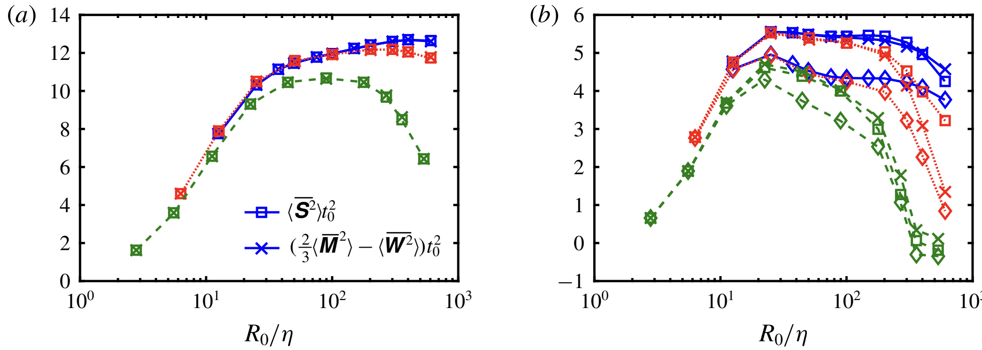

FIGURE 1. Generalized Betchov relations (3.12) and (3.38): (*a*) left-hand side (squares) and right-hand side (crosses) of (3.12); (*b*) negative values of left-hand side (squares) and right-hand side (crosses) of (3.38). The values of $3\langle \overline{\boldsymbol{WSW}}\rangle$ (diamonds) are also shown in (*b*) for comparison. All terms are made dimensionless by using the time scale $t_0 \equiv (R_0^2/\varepsilon)^{1/3}$. In both panels, the results obtained at Reynolds numbers $R_\lambda = 610$, 406 and 166 are shown by the solid blue, red dotted and dark-green dashed lines, respectively.

5. Verification of the theoretical predictions: DNS results

In this section we examine the theoretical results derived in §§ 2–4, using DNS data. In addition to checking our derivation, numerical data provide useful information on T_3^p, the third moments of $\boldsymbol{M}$ (see (3.25)), which depend on a largely undocumented three-point velocity correlation function; see § 3.2.

Three different datasets with Reynolds number $R_\lambda = 166$, 406 and 610 are used. The $R_\lambda = 166$ dataset was generated by using a spectral code, run on the cluster at ENS Lyon with a 384^3 spatial resolution. The other two sets were downloaded from the Johns Hopkins University database (Li *et al.* 2008; Yeung, Donzis & Sreenivasan 2012). In order to construct the PVGT from regular tetrahedra with various sizes, we note that four points out of the eight vertices of a cube form a regular tetrahedron if every two of them are on a surface diagonal line, which provides a convenient approach to extract data points forming tetrahedra from a regular cubic grid out of the simulation domain. The smallest tetrad size $R_{0,min}$ that can be reached is then $\sqrt{2}$ times the grid spacing. Tetrads with sizes in integer numbers of $R_{0,min}$ can also be obtained without interpolation. The eight vertices of a cube form two tetrahedra with different orientations, so the number of tetrahedra that one can construct from N grid points is equal to $2N$, using the periodic boundary conditions of the numerical simulations. For dataset $R_\lambda = 166$ we extract 384^3 data points from two different snapshots, which results in statistics of $2 \times 384^3 \approx 1.1 \times 10^8$ for each orientation and $R_{0,min}/\eta \approx 2.8$. For the other two Reynolds numbers, we extract 512^3 data points from one single snapshot, which allows us to obtain statistics with $512^3 \approx 1.3 \times 10^8$ data points for each orientation and $R_{0,min}/\eta \approx 6.3$ at $R_\lambda = 406$ and $R_{0,min}/\eta \approx 12.5$ at $R_\lambda = 610$. To check the statistical convergence, we compared the values obtained from two different tetrahedron orientations, and in all cases they differ by no more than a few per cent.

Figure 1(*a*) and 1(*b*) verify the generalized Betchov relations, equations (3.12) and (3.38), respectively. Namely, the left-hand (square symbols) and right-hand (cross symbols) sides of (3.12) and (3.38), made dimensionless by using the Kolmogorov time scale corresponding to the tetrad size, $t_0 \equiv (R_0^2/\varepsilon)^{1/3}$, are plotted. For (3.38), we actually plotted the negative values of both sides, as $\langle \overline{\boldsymbol{S}^3}\rangle < 0$. Our results show that

https://doi.org/10.1017/jfm.2020.375 Published online by Cambridge University Press

the two sets of symbols superpose almost perfectly for both second- and third-order quantities. The imbalance between the two sides of the equation, clearly visible at large values of R_0/η in the case of the third-order moments, is very likely to be due to the residual large-scale anisotropy, since the equations have been derived under the explicit assumption of homogeneity and isotropy of the flow. Moreover, we note that, when normalized by t_0, the results at the two higher Reynolds numbers, $R_\lambda = 406$ and 610, collapse well for R_0 smaller than the integral length scale L. This is an indication that the properties of the inertial range dynamics studied here with the PVGT are indeed universal for high-Reynolds-number turbulence. The finite Reynolds-number effect is evident from the systematic variations of the curves when R_λ decreases.

Figure 1(*b*) also shows the values of the term corresponding to vortex stretching, $3\langle\overline{\boldsymbol{WSW}}\rangle$, shown with diamond symbols. One can see that, in the dissipative range, this quantity is identical to $-\langle\overline{\boldsymbol{S}^3}\rangle$ as implied by (3.3). At larger values of R_0, $3\langle\overline{\boldsymbol{WSW}}\rangle$ is only slightly smaller than $-\langle\overline{\boldsymbol{S}^3}\rangle$ (we will return to this ratio; see figure 2*d*). This indicates that the relation between the third moment of strain and vortex stretching, established in (3.3), provides a good approximation even in the inertial range.

Further insight into the generalized Betchov relations can be obtained by comparing the various terms in (3.12) and (3.38). Figure 2(*a*) shows the terms in (3.12), all made dimensionless by dividing by $D_2(R_0)/R_0^2$. The horizontal lines correspond to the exact values in the dissipative or the inertial range, as predicted by the calculations in § 3.1.2; see (3.21)–(3.23). For values of $R_0 \lesssim 4\eta$, the values of $\langle\overline{\boldsymbol{M}}^2\rangle$, $\langle\overline{\boldsymbol{S}^2}\rangle$ and $\langle\overline{\boldsymbol{W}^2}\rangle$ agree with the asymptotic limit predicted in the dissipative range. Similarly, for $R_0 \gtrsim 50\eta$, these quantities follow the predicted behaviour in the inertial range. The relatively small value of $\langle\overline{\boldsymbol{M}}^2\rangle$, compared to either of $\langle\overline{\boldsymbol{S}^2}\rangle$ or $\langle\overline{\boldsymbol{W}^2}\rangle$, ensures that the ratio $-\langle\overline{\boldsymbol{S}^2}\rangle/\langle\overline{\boldsymbol{W}^2}\rangle$ does not deviate by more than ∼30 % with respect to 1. As shown in figure 2(*b*), the ratio $-\langle\overline{\boldsymbol{S}^2}\rangle/\langle\overline{\boldsymbol{W}^2}\rangle$ increases monotonically from 1 in the dissipative range to the predicted value of 35/27 when R_0 increases in the inertial range. We stress that, at the level of the PVGT, for R_0 above the dissipative range, or $R_0 \gtrsim 10\eta$, strain dominates over enstrophy.

The values of $\langle\overline{\boldsymbol{M}}^3\rangle$ and $\langle\overline{\boldsymbol{M}}\,\overline{\boldsymbol{M}}^2\rangle$, made dimensionless by dividing by $D_3(R_0)/R_0^3$, are shown in figure 2(*c*). Note that $D_3(R_0) < 0$, so the positive values in the figure imply that the two quantities shown are in fact negative. As expected from the fact that $\boldsymbol{M}$ reduces to $\boldsymbol{m}$ when R_0 is in the dissipative range, and from incompressibility, the third-order moments of $\boldsymbol{M}$, shown in figure 2(*c*), appear to decay to zero in the dissipative range, for $R_0 \lesssim 4\eta$. On the other hand, for $30\eta \lesssim R_0 \lesssim L$, both $\langle\overline{\boldsymbol{M}}^3\rangle$ and $\langle\overline{\boldsymbol{M}}\,\overline{\boldsymbol{M}}^2\rangle$ approximately show a plateau when $R_\lambda \gtrsim 400$. This is not surprising, since the correlation functions $\mathscr{Q}_i$ in (3.36) are expected to scale with the same exponent as D_3 in the inertial range. In the same spirit, the ratio between $\langle\overline{\boldsymbol{S}^3}\rangle$ and $\langle\overline{\boldsymbol{WSW}}\rangle$ decreases from the theoretical prediction −3 in the dissipative range to another constant value, approximately equal to −3.7, in the inertial range. Although this ratio determined numerically in the inertial range differs slightly from that predicted by the original Betchov relation in the dissipative range, equation (3.3), the qualitative picture is unchanged: the positive value of (perceived) vortex stretching $\langle\overline{\boldsymbol{WSW}}\rangle > 0$, corresponds to $\langle\overline{\boldsymbol{S}^3}\rangle < 0$.

Figure 3 presents the values of the mixed second-order invariants of $\boldsymbol{M}$ and $\boldsymbol{\Pi H}$, determined only from the $R_\lambda = 406$ flow. (The external forcing terms in the $R_\lambda =$ 166 and $R_\lambda = 610$ cases are not available, so making the analysis of the $\boldsymbol{\Pi H}$ term impossible in these two cases.) The smallest value of $R_0 \approx 6.3\eta$ does not allow us to

https://doi.org/10.1017/jfm.2020.375 Published online by Cambridge University Press

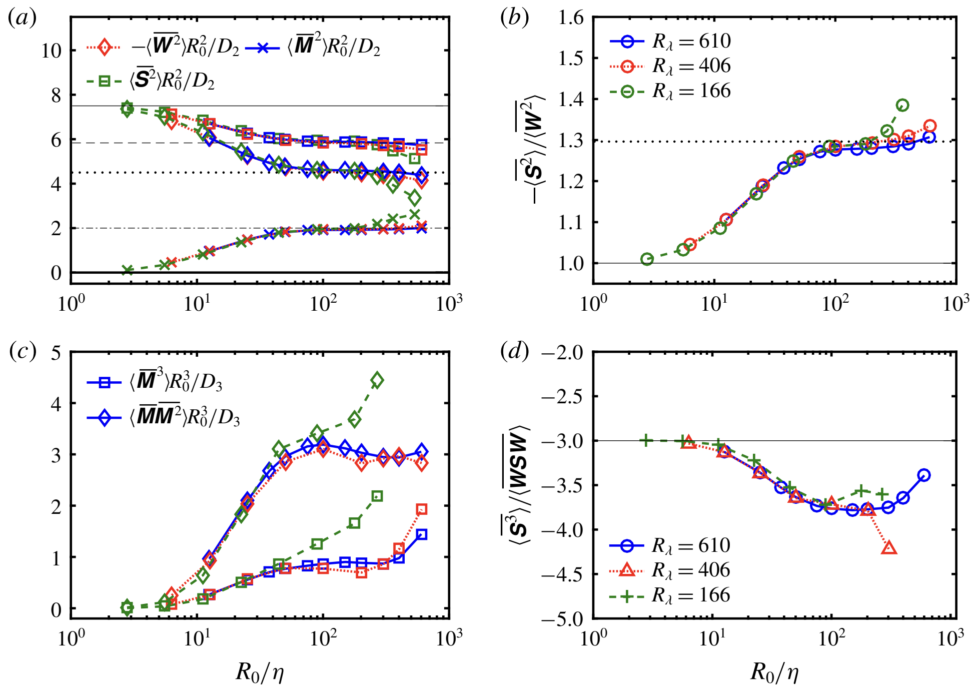

FIGURE 2. The DNS results for the second- and third-order invariants of $\boldsymbol{M}$. In all panels, blue solid, red dotted and dark-green dashed curves indicate Reynolds numbers $R_\lambda = 610$, 406 and 166, respectively. (*a*) Values of $\langle\overline{\boldsymbol{M}}^2\rangle$ (crosses), $-\langle\overline{\boldsymbol{W}^2}\rangle$ (diamonds) and $\langle\overline{\boldsymbol{S}^2}\rangle$ (squares), all normalized by $D_2(R_0)/R_0^2$, at different scale R_0/η. The straight lines show the theoretical predictions: $\langle\overline{\boldsymbol{S}^2}\rangle = -\langle\overline{\boldsymbol{W}^2}\rangle = 15/2$ (thin solid line) and $\langle\overline{\boldsymbol{M}}^2\rangle = 0$ (thick solid line) in the dissipative range, and $\langle\overline{\boldsymbol{S}^2}\rangle = 35/6$ (thin dashed line), $-\langle\overline{\boldsymbol{W}^2}\rangle = 9/2$ (thin dotted line) and $\langle\overline{\boldsymbol{M}}^2\rangle = 2$ (thin dot-dashed line) in the inertial range. (*b*) Change of the ratio $-\langle\overline{\boldsymbol{S}^2}\rangle/\langle\overline{\boldsymbol{W}^2}\rangle$ with R_0/η. The thin solid and the dotted lines show the predicted values of 1 and 35/27 in the dissipative and inertial ranges. (*c*) Values of $\langle\overline{\boldsymbol{M}}^3\rangle$ (squares) and $\langle\overline{\boldsymbol{M}}\,\overline{\boldsymbol{M}^2}\rangle$ (diamonds), normalized by $D_3(R_0)/R_0^3$, at different scale R_0/η. (*d*) Dependence of the ratio $\langle\overline{\boldsymbol{S}^3}\rangle/\langle\overline{\boldsymbol{WSW}}\rangle$ as a function of scale R_0/η. The solid line is the theoretical value -3 in the dissipative range.

explore directly the dissipative range. On the other hand, our results are compatible with the existence of a plateau in the inertial range of scales for $\langle\overline{\boldsymbol{M\Pi H}}\rangle$ and for $\langle\overline{\boldsymbol{M}}\,\overline{\boldsymbol{\Pi H}}\rangle$, consistent with the values predicted; see § 4. The possible existence of a plateau for $\langle\overline{\boldsymbol{M}(\boldsymbol{\Pi H})^{\mathrm{T}}}\rangle$, however, is at best suggested by the inflection point in figure 3.

In figure 3(*b*), (*c*) and (*d*), we decompose the values of the mixed invariants into three parts, corresponding to the force, pressure and viscous terms. Consistent with our previous analysis, when $R_0 \ll L$, the contributions from the external force and the pressure gradient terms are negligible. The situation changes when $R_0 \simeq L$, which is likely to be a consequence of the flow anisotropy at scales comparable to the size of the simulation domain.

Finally, figure 4 shows the terms in the equation for the rate of production of strain and vorticity obtained from PVGT based on regular tetrads, i.e. equations (2.18)

https://doi.org/10.1017/jfm.2020.375 Published online by Cambridge University Press

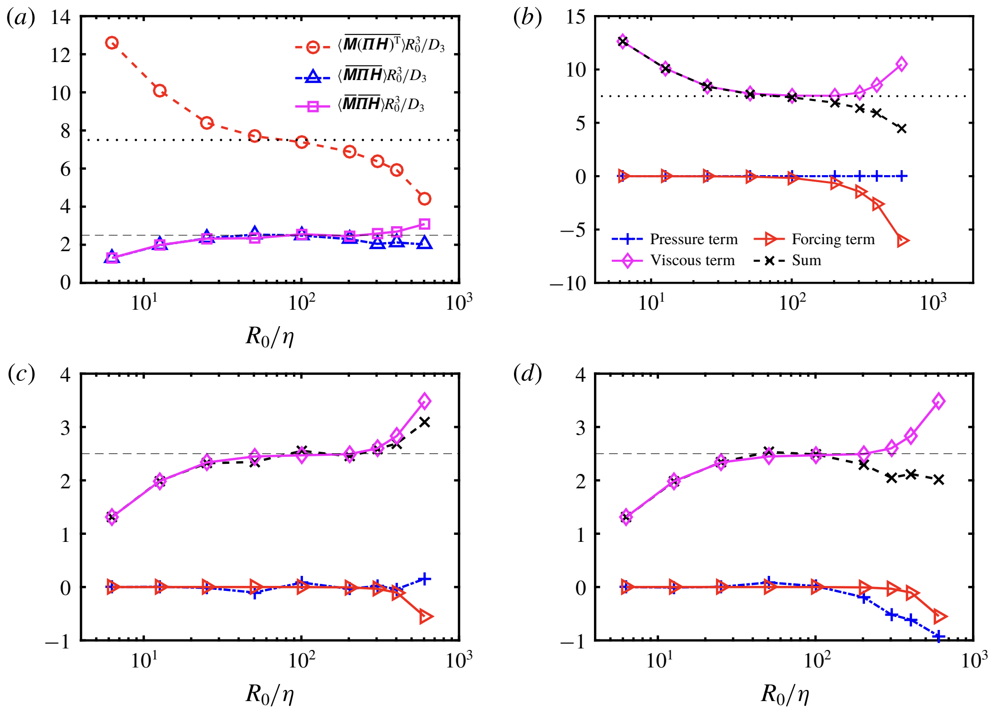

FIGURE 3. The DNS results for the mixed second-order invariants of $\boldsymbol{M}$ and $\overline{\boldsymbol{\Pi H}}$ at $R_\lambda = 406$. (a) Values of $\langle \boldsymbol{M}(\overline{\boldsymbol{\Pi H}})^{\mathrm{T}}\rangle$ (crosses), $\langle \overline{\boldsymbol{M}\boldsymbol{\Pi H}}\rangle$ (pluses) and $\langle \overline{\boldsymbol{M}}\,\overline{\boldsymbol{\Pi H}}\rangle$ (diamonds) normalized by $D_3(R_0)/R_0^3$. (b) Contributions of the pressure gradient term (blue pluses), viscous term (magenta diamonds) and external forcing (black triangles) to $\langle \overline{\boldsymbol{M}(\boldsymbol{\Pi H})^{\mathrm{T}}}\rangle$ and their sum (red crosses), all normalized by $D_3(R_0)/R_0^3$. (c) Same as (b), but for $\langle \overline{\boldsymbol{M}\boldsymbol{\Pi H}}\rangle$. ($d$) Same as ($b$), but for $\langle \overline{\boldsymbol{M}}\,\overline{\boldsymbol{\Pi H}}\rangle$. The straight lines are theoretical predictions in the inertial range for $\langle \overline{\boldsymbol{M}(\boldsymbol{\Pi H})^{\mathrm{T}}}\rangle$ ($= 15/2$, dotted line) and $\langle \overline{\boldsymbol{M}\boldsymbol{\Pi H}}\rangle = \langle \overline{\boldsymbol{M}}\,\overline{\boldsymbol{\Pi H}}\rangle$ ($= 5/2$, dashed line).

and (2.19). Note that the rates of production for quantities from PVGT are non-zero even in statistically stationary turbulence because the tetrads evolve in size and shape as the fluid particles forming the tetrads move in the flow. The data shown in figure 4 are from DNS at $R_\lambda = 406$. All the terms in these two equations are made dimensionless by dividing by $D_3(R_0)/R_0^3$. We multiplied the various contributions by ± 1 to make all the quantities positive (note that $D_3(R_0)$ is negative). As an example, we plot $\langle \overline{\boldsymbol{S}^3}\rangle R_0^3/D_3(R_0)$ instead of $-\langle \overline{\boldsymbol{S}^3}\rangle R_0^3/D_3(R_0)$ that appears in (2.18). Note that since $\langle \overline{\boldsymbol{S}^2}\rangle > 0$ and $\langle \overline{\boldsymbol{W}^2}\rangle < 0$, the DNS data shown in figure 4 indicate that $\mathrm{d}\langle \overline{\boldsymbol{S}^2}\rangle/\mathrm{d}t > 0$ and $\mathrm{d}\langle \overline{\boldsymbol{W}^2}\rangle/\mathrm{d}t < 0$, i.e. the magnitudes of both strain and vorticity are increasing. From figure 4(a), we see that the largest contribution to the production of strain comes from $-\langle \overline{\boldsymbol{S}^3}\rangle$, with additional small positive contribution from the term $-\frac{2}{3}\langle \overline{\boldsymbol{M}}\,\overline{\boldsymbol{S}^2}\rangle$. The term $\langle \overline{\boldsymbol{\Pi H}\boldsymbol{S}}\rangle$, on the other hand, acts against the production of strain. This contribution describes the action of other forces against the deformation of the tetrads, and, as we noted when discussing figure 3, is mostly due to the viscous dissipation. Expressing $\langle \overline{\boldsymbol{\Pi H}\boldsymbol{S}}\rangle = (\langle \overline{\boldsymbol{\Pi H}\boldsymbol{M}}\rangle + \langle \overline{\boldsymbol{\Pi H}\boldsymbol{M}^{\mathrm{T}}}\rangle)/2 - \langle \overline{\boldsymbol{M}\boldsymbol{\Pi H}}\rangle/3$ and using equations (4.16) and (4.17) leads to the prediction that $\langle \overline{\boldsymbol{\Pi H}\boldsymbol{S}}\rangle \times R_0^3/D_3 = 25/6$ in the

https://doi.org/10.1017/jfm.2020.375 Published online by Cambridge University Press

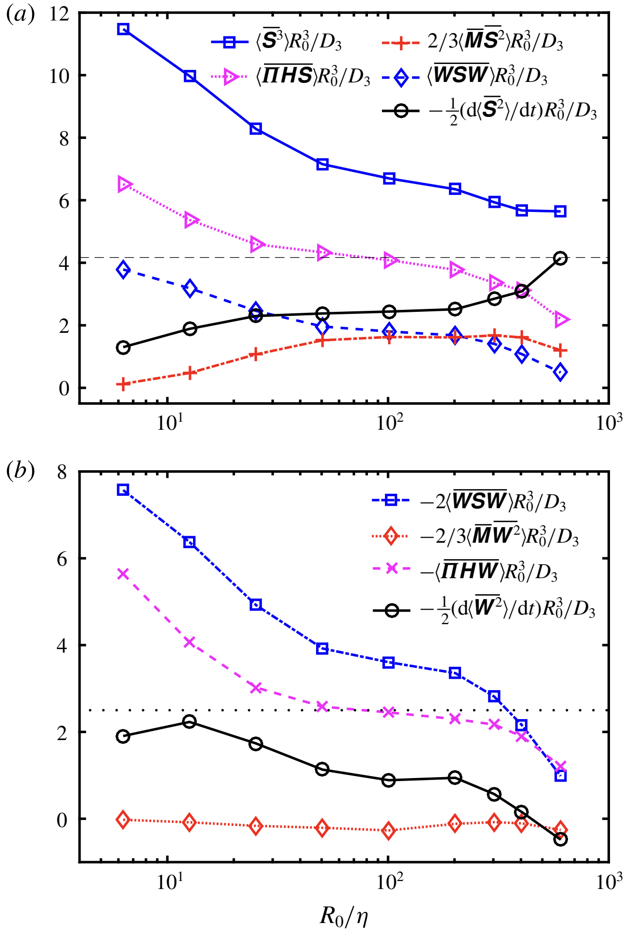

FIGURE 4. Magnitudes of terms in the equation for the rate of production of (*a*) strain, equation (2.18), and (*b*) vorticity, equation (2.19). All terms are made dimensionless by dividing by $D_3(R_0)/R_0^3$ (note that $D_3(R_0) < 0$). The dashed horizontal line in panel (*a*) is the theoretical prediction in the inertial range for $\langle \overline{\boldsymbol{\Pi H S}}\rangle$ $(= 25/6)$, and the dotted horizontal line in panel (*b*) is the prediction for $\langle \overline{\boldsymbol{\Pi H W}}\rangle$ $(= 5/2)$.

inertial range, which is well supported by the data shown in figure 4(*a*). In addition, the vortex stretching term, $\langle \overline{\boldsymbol{WSW}}\rangle$, also provides a negative contribution to the rate of change of $\langle \overline{\boldsymbol{S}}^2\rangle$.

Figure 4(*b*) shows all the contributions to the equation of evolution of enstrophy, equation (2.19). As expected, the main positive contribution is the vortex stretching term $\langle \overline{\boldsymbol{WSW}}\rangle$. The term originating from the non-zero value of $\overline{\boldsymbol{M}}$, $-\frac{2}{3}\langle \overline{\boldsymbol{M}}\,\overline{\boldsymbol{W}}^2\rangle$, is negligibly small over the entire range of R_0 explored. In the inertial range, the forcing term $\langle \overline{\boldsymbol{\Pi H W}}\rangle$ can be expressed, by using (4.2), and by substituting the expressions (4.16) and (4.17), as

$$-\langle \overline{\boldsymbol{\Pi H W}}\rangle = \frac{1}{2}(\langle \overline{\boldsymbol{M}(\boldsymbol{\Pi H})^{\mathrm{T}}}\rangle - \langle \overline{\boldsymbol{M \Pi H}}\rangle) = \frac{1}{2}\left(\frac{15}{2} - \frac{5}{2}\right)\frac{D_3}{R_0^3} = \frac{5}{2}\frac{D_3}{R_0^3} = -\frac{2\varepsilon}{R_0^2}. \quad (5.1)$$

https://doi.org/10.1017/jfm.2020.375 Published online by Cambridge University Press

This can be rewritten as $-\langle\overline{\boldsymbol{\Pi}\boldsymbol{H}\boldsymbol{W}}\rangle R_0^3/D_3 = \frac{5}{2}$. This predicted value is in very good agreement with the numerical data shown in figure 4(*b*). Consistent with the notion that a positive vortex stretching is a part of the turbulent cascade, we observe that the generation of perceived enstrophy is positive. As a consequence, $-\langle\overline{\boldsymbol{S}^3}\rangle$ should be greater than zero, which says that the intermediate eigenvalue of $\boldsymbol{S}$ is preferentially positive.

As the terms in the equation for the rate of production of strain and vorticity, $\frac{1}{2}\,\mathrm{d}\langle\overline{\boldsymbol{S}^2}\rangle/\mathrm{d}t$ and $-\frac{1}{2}\,\mathrm{d}\langle\overline{\boldsymbol{W}^2}\rangle/\mathrm{d}t$, are shown in the two panels of figure 4 with the same normalization, they could thus be compared directly. We note that, except in the dissipative range when $R_0 \lesssim \eta$, strain production is much larger than enstrophy production, approximately by a factor of 3 in the inertial range. (Note that the vertical ranges of the two panels are different.) As already noted, the evolution of strain and enstrophy measured with regular tetrads of size R_0 does not give rise to a closed, stationary problem, as the shape and size of the tetrads evolve with time, an effect that has to be taken into account in a consistent description of the problem (Pumir *et al.* 2013). The excess of strain production, compared to that of vorticity production, is nonetheless consistent with the excess of strain over enstrophy when R_0 is in the inertial range, as clearly seen in our prediction (3.23) and from data shown in figure 2(*b*). Thus, our results at a finite scale, with R_0 in the inertial range, consistently point to an excess of strain, compared to enstrophy.

6. Discussion and concluding remarks

In this article, we have established exact equations for the evolution of the perceived velocity gradient tensor (PVGT), $\boldsymbol{M}$, constructed from four points in the fluid, forming a tetrahedron of size R_0 in a homogeneous turbulent flow. Starting from the incompressible Navier–Stokes equations, we derived the evolution equation of the rate of strain and enstrophy of the PVGT. One important aspect in the present work is that we explicitly took into account the trace of $\boldsymbol{M}$, which is not identically zero when the size of the tetrad is outside the dissipative range. The usual decomposition of $\boldsymbol{M}$ in terms of its symmetric, $\boldsymbol{S}$, and antisymmetric, $\boldsymbol{W}$, components has to be generalized to take into account the non-zero $\overline{\boldsymbol{M}} \equiv \mathrm{tr}(\boldsymbol{M})$; see (2.5).

We extended the well-known Betchov relations between invariants of the velocity gradient tensor, $\boldsymbol{m}$, to the PVGT $\boldsymbol{M}$. While the Betchov relations were originally derived under the assumptions that the flow is homogeneous and incompressible, our extension requires a further assumption of isotropy, and, in addition, we restrict ourselves to the PVGT $\boldsymbol{M}$ constructed from four points forming a regular tetrad with lateral size R_0. The extended Betchov relations allowed us to relate the norms of strain $\langle\overline{\boldsymbol{S}^2}\rangle$ and enstrophy $-\langle\overline{\boldsymbol{W}^2}\rangle$ in the flow, as well as vortex stretching $\langle\overline{\boldsymbol{W}\boldsymbol{S}\boldsymbol{W}}\rangle$ and the third moment of strain, $\langle\overline{\boldsymbol{S}^3}\rangle$, defined at any scale R_0. Our analytic results are confirmed by DNS results for homogeneous and isotropic flows. When R_0 is in the inertial range, the ratio $-\langle\overline{\boldsymbol{S}^2}\rangle/\langle\overline{\boldsymbol{W}^2}\rangle$ is approximately 1.3 (compared to 1 in the dissipative range, see figure 2*b*), in excellent agreement with our theoretical value of 35/27 (see (3.23)). We also demonstrated numerically that, in the inertial range of scales, the production of strain significantly exceeds that of enstrophy.

In technical terms, our derivation consists in reducing the moments of order up to three of the PVGT, based on four points forming a regular tetrahedron, to elementary two- and three-point velocity correlations/structure functions. In the case of homogeneous and isotropic turbulence, while the two-point correlations

https://doi.org/10.1017/jfm.2020.375 Published online by Cambridge University Press

and structure functions have been extensively studied, theoretically, numerically and experimentally, much less is known about the correlation function of velocities involving three different points. Our analysis of the third moment of $\boldsymbol{M}$ requires some information about the three-point velocity correlation for three points forming an equilateral triangle. We hope that our work can motivate further investigation of these three-point velocity correlations and structure functions (Mydlarski *et al.* 1998; Yao *et al.* 2014; Wu *et al.* 2018).

The generalization of the Betchov relations to the PVGT for scales R_0 in the inertial range of turbulent flows allows us to draw interesting conclusions on the relative role of strain and vorticity in the case of homogeneous and isotropic flows. These results, taken together, suggest the prevalence of strain over vorticity at the level of $\boldsymbol{M}$, an effect anticipated several times (Tsinober 2009), and recently studied using alternative approaches (Carbone & Bragg 2020; Johnson 2020). The description in terms of the PVGT may therefore lead to insight previously difficult to obtain, at the inertial range of scales. A challenging question would be to understand whether the results derived by algebraic manipulations of the equations obtained here could be understood from elementary terms, as the evolution of a tetrahedron is simply due to turbulent transport.

The general approach discussed here offers several interesting possibilities of extension. In this work, we have derived general equations for $\boldsymbol{M}$, valid without any particular condition on the flow except homogeneity. It would be interesting to study flows with a non-trivial large-scale structure, such as a shear or straining. A good control on how the large-scale structure of the flow affects the properties of $\boldsymbol{M}$ at smaller scales is of interest not only for fundamental reasons, but also for improving large-eddy simulation strategies (Meneveau & Katz 2000).

Acknowledgements

We acknowledge financial support from the National Science Foundation of China (NSFC) under grant no. 11672157. A.P. received support from the IDEXLyon project (Contract no. ANR-16-IDEX-0005) under University of Lyon auspices. We are very grateful to A. Bragg for many fruitful discussions.

Declaration of interests

The authors report no conflict of interest.

REFERENCES

BETCHOV, R. 1956 An inequality concerning the production of vorticity in isotropic turbulence. *J. Fluid Mech.* **1**, 497–504.

BIFERALE, L., BOFFETTA, G., CELANI, A., DEVENISH, B. J., LANOTTE, A. & TOSCHI, F. 2005 Multiparticle dispersion in fully developed turbulence. *Phys. Fluids* **17**, 111701.

BODENSCHATZ, E., BEWLEY, G. P., NOBACH, H., SINHUBER, M. & XU, H. 2014 Variable density turbulence tunnel facility. *Rev. Sci. Instrum.* **85**, 093908.

BORUE, V. & ORSZAG, S. A. 1998 Local energy flux and subgrid-scale statistics in three-dimensional turbulence. *J. Fluid Mech.* **336**, 1–31.

BUARIA, D., PUMIR, A., BODENSCHATZ, E. & YEUNG, P. K. 2019 Extreme velocity gradients in turbulent flows. *New J. Phys.* **21**, 043004.

CARBONE, M. & BRAGG, A. D. 2020 Is vortex stretching the main cause of the turbulent energy cascade? *J. Fluid Mech.* **883**, R2.

https://doi.org/10.1017/jfm.2020.375 Published online by Cambridge University Press

CHERTKOV, M., PUMIR, A. & SHRAIMAN, B. I. 1999 Lagrangian tetrad dynamics and the phenomenology of turbulence. *Phys. Fluids* **11**, 2394–2410.

CHEVILLARD, L. & MENEVEAU, C. 2006 Lagrangian dynamics and statistical geometric structure of turbulence. *Phys. Rev. Lett.* **97**, 174501.

COMTE-BELLOT, G. & CORRSIN, S. 1966 The use of a contraction to improve the isotropy of grid-generated turbulence. *J. Fluid Mech.* **25**, 657–682.

DAVIDSON, P. A. 2015 *Turbulence: An Introduction for Scientists and Engineers*, 2nd edn. Oxford University Press.

DEVENISH, B. J. 2013 Geometrical properties of turbulent dispersion. *Phys. Rev. Lett.* **110**, 064504.

DEVENISH, B. J. & THOMSON, D. J. 2013 A Lagrangian stochastic model for tetrad dispersion. *J. Turbul.* **14**, 107–120.

DOUADY, S., COUDER, Y. & BRACHET, M. E. 1991 Direct observation of the intermittency of intense vorticity filaments in turbulence. *Phys. Rev. Lett.* **67**, 983–986.

FRISCH, U. 1995 *Turbulence: The Legacy of A. N. Kolmogorov*. Cambridge University Press.

HACKL, J. F., YEUNG, P. K. & SAWFORD, B. L. 2011 Multi-particle and tetrad statistics in numerical simulations of turbulent relative dispersion. *Phys. Fluids* **23** (6), 065103.

ISHIHARA, T., KANEDA, Y., YOSOKAWA, M., ITAKURA, K. & UNO, A. 2007 Small-scale statistics in high resolution of numerically isotropic turbulence. *J. Fluid Mech.* **592**, 335–366.

JIMENEZ, J., WRAY, A. A., SAFFMAN, P. G. & ROGALLO, R. S. 1993 The structure of intense vorticity in isotropic turbulence. *J. Fluid Mech.* **255**, 65–90.

JOHNSON, P. L. 2020 Energy transfer from large to small scales in turbulence by multi-scale nonlinear strain and vorticity interaction. *Phys. Rev. Lett.* **124**, 104501.

JOHNSON, P. L. & MENEVEAU, C. 2016 A closure for Lagrangian velocity gradient evolution in turbulence using recent-deformation mapping of initially Gaussian field. *J. Fluid Mech.* **804**, 387–419.

JOHNSON, P. L. & MENEVEAU, C. 2018 Predicting viscous-range velocity gradient dynamics in large-eddy simulations of turbulence. *J. Fluid Mech.* **837**, 80–114.

JUCHA, J., XU, H., PUMIR, A. & BODENSCHATZ, E. 2014 Time-reversal-symmetry breaking in turbulence. *Phys. Rev. Lett.* **113**, 054501.

VON KÁRMÁN, T. & HOWARTH, L. 1938 On the statistical theory of isotropic turbulence. *Proc. R. Soc. Lond.* A **164**, 192–215.

LI, Y., PERLMAN, E., WAN, M., YANG, Y., MENEVEAU, C., BURNS, R., CHEN, S., SZALAY, A. & EYINK, G. L. 2008 A public turbulence database cluster and applications to study Lagrangian evolution of velocity increments in turbulence. *J. Turbul.* **9** (N31), 1–29.

LÜTHI, B., OTT, S., BERG, J. & MANN, J. 2007 Lagrangian multi-particle statistics. *J. Turbul.* **8** (N45), 1–17.

MENEVEAU, C. 2011 Lagrangian dynamics and models of the velocity gradient tensor in turbulent flows. *Annu. Rev. Fluid Mech.* **43**, 219–245.

MENEVEAU, C. & KATZ, J. 2000 Scale-invariance and turbulence models for large-eddy simulation. *Annu. Rev. Fluid Mech.* **32**, 1–32.

MENEVEAU, C. & LUND, T. S. 1994 On the Lagrangian nature of the turbulence energy cascade. *Phys. Fluids* **6**, 2820–2825.

MONIN, A. S. & YAGLOM, A. M. 1975 *Statistical Fluid Mechanics*. Cambridge University Press.

MYDLARSKI, L., PUMIR, A., SHRAIMAN, B. I., SIGGIA, E. D. & WARHAFT, Z. 1998 Structures and multipoint correlators for turbulent advection: predictions and experiments. *Phys. Rev. Lett.* **81**, 4373–4376.

NASO, A. 2019 Multiscale analysis of the structure of homogeneous turbulence. *Phys. Rev. Fluids* **4**, 024609.

NASO, A. & GODEFERD, F. S. 2012 Statistics of the perceived velocity gradient tensor in a rotating turbulent flow. *New J. Phys.* **14**, 125002.

NASO, A. & PUMIR, A. 2005 Scale dependence of the coarse-grained velocity derivative tensor structure in turbulence. *Phys. Rev.* E **72**, 056318.

POPE, S. B. 2000 *Turbulent Flows*. Cambridge University Press.

https://doi.org/10.1017/jfm.2020.375 Published online by Cambridge University Press

PUMIR, A., BODENSCHATZ, E. & XU, H. 2013 Tetrahedron deformation and alignment of perceived vorticity and strain in a turbulent flow. *Phys. Fluids* **25**, 035101.

PUMIR, A., SHRAIMAN, B. I. & CHERTKOV, M. 2000 Geometry of Lagrangian dispersion in turbulence. *Phys. Rev. Lett.* **85** (25), 5324–5327.

SAWFORD, B. L., POPE, S. B. & YEUNG, P. K. 2013 Gaussian Lagrangian stochastic models for multi-particle dispersion. *Phys. Fluids* **25**, 055101.

SIGGIA, E. 1981 Numerical study of small-scale intermittency in three-dimensional turbulence. *J. Fluid Mech.* **107**, 357–406.

TAO, B., KATZ, J. & MENEVEAU, C. 2002 Statistical geometry of subgrid-scale stresses determined from holographic particle image velocimetry measurements. *J. Fluid Mech.* **457**, 35–78.

TOWNSEND, A. A. 1951 On the fine-scale structure of turbulence. *Proc. R. Soc. Lond.* A **208**, 534–542.

TSINOBER, A. 2009 *An Informal Conceptual Introduction to Turbulence*. Springer.

VAN DER BOS, F., TAO, B., MENEVEAU, C. & KATZ, J. 2002 Effects of small-scale turbulent motions on the filtered velocity gradient tensor as deduced from holographic particle image velocimetry measurements. *Phys. Fluids* **14**, 2456–2474.

WU, J. Z., FANG, L., SHAO, L. & LU, L. P. 2018 Theories and applications of second-order correlation of longitudinal velocity increments at three points in isotropic turbulence. *Phys. Lett.* A **382**, 1665–1671.

XU, H., OUELLETTE, N. T. & BODENSCHATZ, E. 2008 Evolution of geometric structures in intense turbulence. *New J. Phys.* **10**, 013012.

XU, H., PUMIR, A. & BODENSCHATZ, E. 2011 The pirouette effect in turbulent flows. *Nat. Phys.* **7**, 709–712.

XU, H., PUMIR, A. & BODENSCHATZ, E. 2016 Lagrangian view of time irreversibility of fluid turbulence. *Sci. China-Phys. Mech. Astron.* **59** (1), 614702.

YAO, S. Y., FANG, L., LV, J. M., WU, J. Z. & LU, L. P. 2014 Multiscale three-point velocity increment correlation in turbulent flows. *Phys. Lett.* A **378**, 885–891.

YEUNG, P. K., DONZIS, D. A. & SREENIVASAN, K. R. 2012 Dissipation, enstrophy and pressure statistics in turbulence simulations at high Reynolds numbers. *J. Fluid Mech.* **700**, 5–15.

https://doi.org/10.1017/jfm.2020.375 Published online by Cambridge University Press